Key Points:
- Bayesian inversion with physics-based models combines diverse data to resolve conduit properties
- Low dome porosity requires low total volatile content and a narrow range of magma permeability
- Exit velocity and flux cause trade-offs among chamber pressure, conduit friction, and radius

Correspondence to:
Y. Q. Wong,
yqwong@stanford.edu

Constraining the Magmatic System at Mount St. Helens (2004–2008) Using Bayesian Inversion With Physics-Based Models Including Gas Escape and Crystallization

Ying-Qi Wong[1] , Paul Segall[1] , Andrew Bradley[2], and Kyle Anderson[3]

[1]Department of Geophysics, Stanford University, Stanford, CA, USA, [2]Center for Computing Research, Sandia National Laboratories, Albuquerque, NM, USA, [3]U.S. Geological Survey, Menlo Park, CA, USA

Abstract Physics-based models of volcanic eruptions track conduit processes as functions of depth and time. When used in inversions, these models permit integration of diverse geological and geophysical data sets to constrain important parameters of magmatic systems. We develop a 1-D steady state conduit model for effusive eruptions including equilibrium crystallization and gas transport through the conduit and compare with the quasi-steady dome growth phase of Mount St. Helens in 2005. Viscosity increase resulting from pressure-dependent crystallization leads to a natural transition from viscous flow to frictional sliding on the conduit margin. Erupted mass flux depends strongly on wall rock and magma permeabilities due to their impact on magma density. Including both lateral and vertical gas transport reveals competing effects that produce nonmonotonic behavior in the mass flux when increasing magma permeability. Using this physics-based model in a Bayesian inversion, we link data sets from Mount St. Helens such as extrusion flux and earthquake depths with petrological data to estimate unknown model parameters, including magma chamber pressure and water content, magma permeability constants, conduit radius, and friction along the conduit walls. Even with this relatively simple model and limited data, we obtain improved constraints on important model parameters. We find that the magma chamber had low (<5 wt %) total volatiles and that the magma permeability scale is well constrained at ∼ $10^{-11.4}$ m^2 to reproduce observed dome rock porosities. Compared with previous results, higher magma overpressure and lower wall friction are required to compensate for increased viscous resistance while keeping extrusion rate at the observed value.

1. Introduction

Ground deformation, seismic activity, gas geochemistry, and petrologic data are all vital for monitoring active volcanoes, yet even today, comparisons among different data types tend to be qualitative rather than quantitative, potentially making interpretations of separate data sets difficult to reconcile. At the same time, physics-based models of volcanic eruptions have become more sophisticated, enabling us to relate physical and chemical properties of magmatic systems to explain the rich observations at the surface and understand how parameters of the magmatic system dictate eruption characteristics such as mass effusion rate and explosivity. These models enhance our ability to interpret observations at volcanoes by offering opportunities to integrate diverse volcanological data sets.

Physics-based conduit flow models track the evolution of magma properties such as density, viscosity, and compressibility through time and space (e.g., Gonnermann & Manga, 2007; Jaupart and Allègre, 1991; Kozono and Koyaguchi, 2012; Mastin, 2002; Melnik and Sparks, 2005). Since these properties depend on constituent phase concentrations of the magma, conduit flow models must account for phase transitions during ascent, including crystallization and gas exsolution. Some studies also consider mass exchange with the surroundings, such as gas loss from the conduit (Collombet, 2009; Kozono & Koyaguchi, 2010, 2012; Jaupart & Allègre, 1991; Melnik & Sparks, 1999). Comparing predictions from these models with observations can inform us about otherwise inaccessible aspects of the magmatic system (Sparks, 2003); however, few studies relate observations to models in a quantitative inverse procedure.

Previous work by Anderson and Segall (2011) developed a physics-based forward model for effusive silicic volcanic eruptions that was subsequently applied in quantitative inversions of geodetic and extrusion data. The model consists of a one-dimensional, radially averaged, isothermal conduit which connects the magma chamber to the surface and is coupled with the elastic surroundings to infer surface displacements arising from conduit normal and shear tractions in addition to changes in magma chamber pressure. As magma ascends, gases exsolve, inducing changes in magma viscosity, calculated using the melt model from Hess and Dingwell (1996). For simplicity, magma was assumed to crystallize into a solid plug at a specified depth. Since this model tracks the time evolution of magmatic properties, it is able to predict time-dependent surface observations (e.g., ground deformation, erupted flux, and gas emissions) in a physically consistent manner. Anderson and Segall (2013) applied the forward model in a Bayesian inverse procedure, using observations from the 2004–2008 dome-forming eruption at Mount St. Helens to infer parameters of interest that are otherwise difficult to constrain, including total magma chamber volume, initial chamber pressure, and volatile content.

To further develop the potential of physics-based inversions of volcanic eruption data, we seek to improve the forward model by implementing equilibrium crystallization and gas transport (water and carbon dioxide) in the conduit to more realistically emulate phase changes. These processes have been shown to produce nonlinear effects that predict a rich range of volcanic behavior (Kozono & Koyaguchi, 2012; Schneider et al., 2012). In particular, Schneider et al. (2012) found that slight changes in temperature and lateral gas escape were responsible for the different eruption regimes observed at Mount St. Helens in the 1980s and in 2004–2008. We include here both lateral and vertical gas transport through the conduit. Additionally, we refine the model for magma rheology by applying the dacite melt model of Whittington et al. (2009) and allowing gradual, pressure-dependent crystallization to influence viscosity. Finally, we include a natural rheological transition between distributed viscous flow and localized frictional sliding along the margins of the solid plug, following Schneider et al. (2012), to emulate the common observation of semisolid plugs in effusive dome-forming eruptions.

In this paper, we examine solutions to the steady state system of equations to understand the effects of these model changes and to derive insight into complicated time-dependent behavior, which will be studied in future work. As in Anderson and Segall (2013), we maintain a relatively simple radially averaged representation of the conduit to allow the forward model to be evaluated a large number of times in a Bayesian inversion. We specifically apply this model to the 2004–2008 dome-forming eruption of Mount St. Helens, focusing on the quasi-steady extrusion period between March and December 2005. We show how additions to the conduit model allow us to constrain new properties of the magmatic system, as well as to understand how different model parameters influence the observed data. Results from this study will inform future analysis of the time-dependent system which will include GPS and extrusion flux time series.

2. Physics-Based Forward Model

The forward model consists of a one-dimensional, isothermal, cylindrical conduit coupled to a magma chamber, following Anderson and Segall (2011) (Figure 1). The magma chamber is treated as a lumped parameter, where only conditions at the chamber top (corresponding to the base of the conduit) are employed to solve the conduit equations. If this pressure exceeds magmastatic pressure, magma will exit the chamber and flow to the surface (the magma has no Bingham yield strength in the current implementation). As magma ascends and depressurizes, crystallization and gas exsolution occur. Both processes increase the bulk magma viscosity. Once viscous resistance to flow exceeds the rate-dependent frictional strength on the conduit wall, the magma forms a solid plug moving primarily through frictional slip on the conduit margin.

2.1. Conservation Laws

Momentum balance for conduit magma is modeled assuming laminar Poiseuille flow through a long cylindrical conduit (e.g., Anderson and Segall, 2011). To simplify the problem to 1-D in depth, the magma velocity is integrated over the conduit cross section to obtain the total flux; dividing by area yields the radially averaged velocity. Typically, Poiseuille flow assumes no slip on the boundary walls; however, we allow frictional slip on the conduit wall using the regularized rate-dependent friction law of Rice et al. (2001) but without state
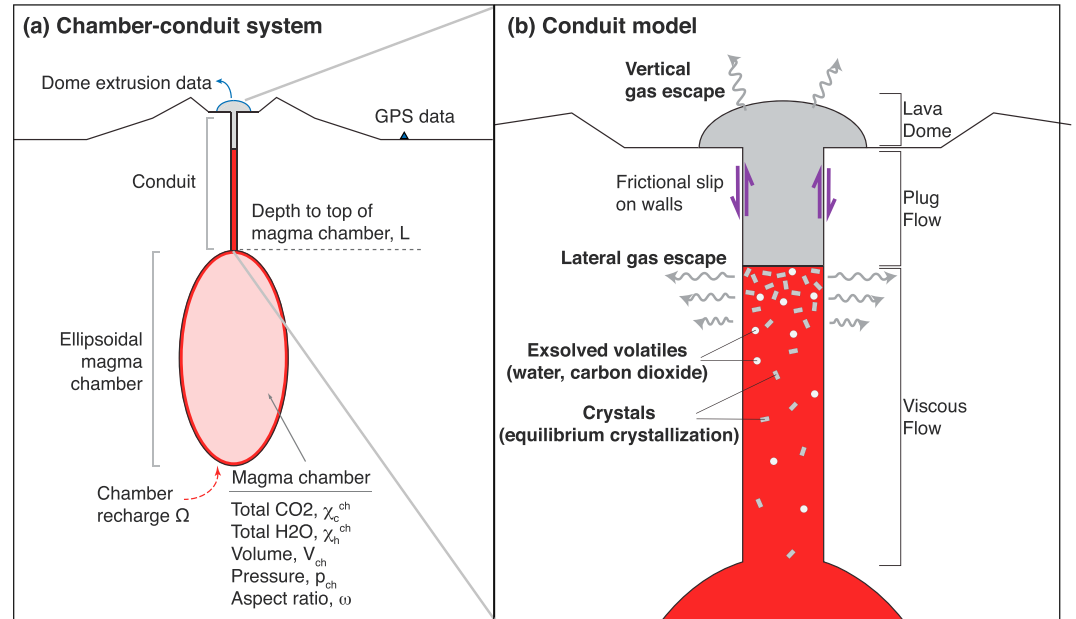
Figure 1. Model geometry and setup. (a) The magma chamber and conduit geometry adapted from Anderson and Segall (2013). Properties of the magma chamber are taken as bulk averages. (b) Details of the conduit model. During ascent, magma crystallizes, volatiles exsolve, and gas escapes laterally and vertically once the percolation threshold is reached. Magma flows as a viscous fluid with frictional sliding on the conduit walls. Initially, flow is dominantly viscous but eventually transitions to frictional sliding.

evolution effects since we focus here on steady state behavior. The radially averaged velocity v is thus the sum of the distributed Newtonian viscous contribution and the contribution from slip along the conduit margin,

$$v = v_{\text{visc}} + v_{\text{fric}} = \frac{\tau_R R}{4\eta} + 2v_r \left[\exp\left(-\frac{f_0}{a} \right) \right] \sinh\left(\frac{\tau_R}{a\sigma_c} \right), \tag{1}$$

where τ_R is the shear stress along the conduit walls,

$$\tau_R = -\frac{R}{2} \left(\frac{\partial p}{\partial z} + \rho g \right). \tag{2}$$

The vertical pressure gradient is $\partial p/\partial z$, ρ is the magma bulk density, which includes liquid, solid, and gas phases, and g is gravitational acceleration. The conduit has radius R, η is the bulk magma viscosity, and σ_c is the effective normal stress on the conduit wall, which is the difference between lithostatic normal stress $\sigma = \rho_{\text{rock}} gz$ and hydrostatic pore pressure p_{hyd}. The friction parameters are the nominal coefficient f_0, rate dependence a, and reference velocity v_r (see Table 1 for symbols used in this paper).

In equation (1), we specify parameter values for R, f_0, and a while assuming a reference frictional velocity $v_r = 10^{-5}$ m/s, representative of the magma extrusion rate at Mount St. Helens in 2005. Finally, η, p, and ρ are dependent variables solved in the model. Bulk viscosity η consists of the dacitic melt viscosity from Whittington et al. (2009) and the effect of magma solid fraction and strain rate (Caricchi et al., 2007; Costa, 2005).

Deep in the conduit, magma viscosity is low ($\sim 10^6$ Pa s), and normal stress on the conduit walls is high, making $v_{\text{visc}} \gg v_{\text{fric}}$ so that magma flows viscously. At shallower depths, magma viscosity is high ($\sim 10^{18}$ Pa s), and normal stress on the conduit walls is diminished, allowing v_{fric} to dominate, and magma slides as a solid plug along the conduit walls. Between these two extremes, both viscous flow and frictional sliding occur and are combined to obtain the total magma velocity. We define the plug to be formed when $v_{\text{fric}} > v_{\text{visc}}$, which corresponds to the peak in wall shear stress.

The continuity equations for liquids and solids, water, and carbon dioxide respectively are given by

$$\frac{\partial}{\partial t}(\rho_l \phi_l + \rho_s \phi_s) + \frac{\partial}{\partial z}[(\rho_l \phi_l + \rho_s \phi_s)v] = 0 \tag{3}$$

Table 1
Symbols Used in System of Equations

| Symbol	Description	Equation or reference value
Fixed constants		
g	Gravitational acceleration	$9.81\ \text{m s}^{-2}$
R_w, R_c	Gas constants for H_2O and CO_2	$461.5, 188.9\ \text{J kg}^{-1}\ \text{K}^{-1}$
Prescribed parameters		
k_{wall}^{top}	Wall rock permeability at surface	$10^{-14}\ \text{m}^2$
L	Conduit length	$3.5\ \text{km}$
T	Temperature of magma	$850°C$
v_r	Reference velocity for friction	$10^{-5}\ \text{m s}^{-1}$
η_g	Gas viscosity	$10^{-4}\ \text{Pa s}$
λ	Length scale for pressure drop from p to far-field p_{hyd}	$2R$
ρ_l, ρ_s	Phase densities in magma (liquid melt, solid)	$2{,}200$ and $2{,}600\ \text{kg m}^{-3}$
ρ_h^d, ρ_c^d	Density of dissolved volatiles (H_2O, CO_2)	$2{,}200\ \text{kg m}^{-3}$
ρ_{rock}	Density of host rock	$2{,}700\ \text{kg m}^{-3}$
Model parameters in Bayesian inversion		Range of uniform part
p_{ch}	Pressure at the top of magma chamber	$75-100\ \text{MPa}$
χ_h^{ch}	Total mass fraction of water relative to melt at the top of magma chamber	$3-7\ \text{wt \%}$
k_c	Scaling parameter for magma permeability	$10^{-15}-10^{-5}\ \text{m}^2$
ϕ_{gc}	Percolation threshold	$0.2-0.4$
f_0	Nominal coefficient of friction	$0.01-0.6$
a	Rate dependence of friction	$10^{-2.2}-10^{-1.8}$
R	Conduit radius	$50-200\ \text{m}$
Dependent variables solved in numerical solution		
m_h	Mole fraction of H_2O	
p	Magma pressure	
v	Magma velocity	
ϕ_g	Gas volume fraction	
Other dependent variables		
k_{mag}, k_{wall}	Component permeabilities (magma, wall rock)	Equation (12), Manning and Ingebritsen (1999)
k_{lat}, k_{vert}	Permeability (lateral, vertical)	Equations (12) and (13)
m_c	Mole fraction of CO_2	$1 - m_h$
p_{hyd}	Pore pressure in the crust	$\rho_{water} g z$
u_g, v_g	Gas velocity (lateral, vertical)	Equation (11)
v_{visc}, v_{fric}	Magma velocity components (viscous, frictional)	Equation (1)
$\dot{\gamma}$	Magma strain rate	$2v/R$
Γ	Ratio of mass concentrations of exsolved CO_2 to H_2O	χ_c^e / χ_h^e
η	Bulk magma viscosity	Equation (8)
η_m	Melt viscosity	Whittington et al. (2009)
η_s	Viscosity increase due to solids	Costa (2005); Caricchi et al. (2007)
ρ	Bulk magma density	Equation (7)
ρ_g	Gas density	Ideal gas law
σ, σ_c	Normal stress (lithostatic, effective)	Lithostatic: $\rho_{rock} g z$
τ_R	Shear stress along conduit wall	Equation (2)
$\phi_l, \phi_s, \phi_h^d, \phi_c^d$	Volume fraction (liquid melt, solid, dissolved H_2O and CO_2)	Equation (6)
$\chi_h^d, \chi_c^d; \chi_h^e, \chi_c^e$	Mass concentration of dissolved and exsolved H_2O and CO_2	Equation (9)
χ_s^{nv}	Mass fraction of solids relative to nonvapor phases (solids and melt)	Schneider et al. (2012)
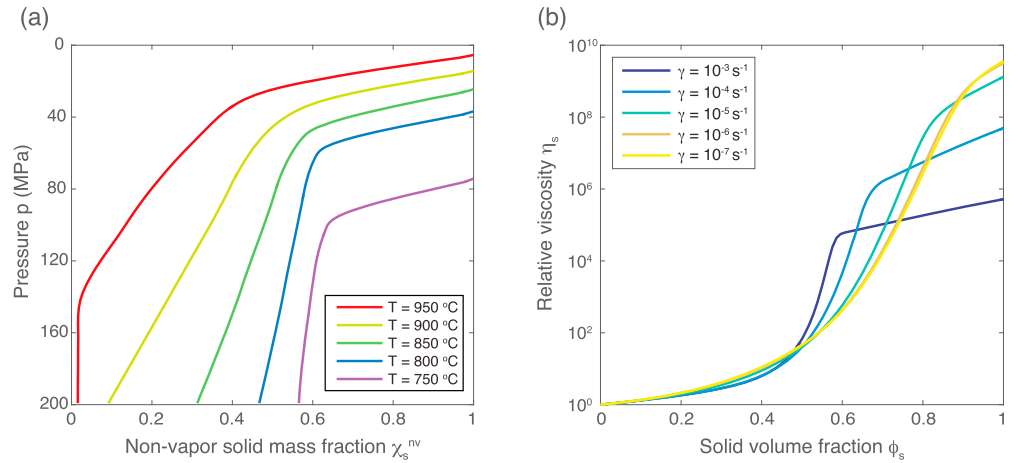
Figure 2. (a) Nonvapor solid mass fraction as a function of pressure for different temperatures, from Schneider et al. (2012). Isothermal conduit flow is assumed, permitting solid mass fraction to be computed as a function of pressure at each depth in the conduit. (b) Relative viscosity due to crystals $\eta_s = \eta/\eta_m$ calculated using the empirical relation of Costa (2005). Fitting parameters in the empirical equation are calculated in terms of shear strain rate $\dot{\gamma}$ (Caricchi et al., 2007).

$$\frac{\partial}{\partial t}\left(\chi_h^d \rho_l \phi_l + \frac{1}{1+\Gamma}\rho_g \phi_g\right) + \frac{\partial}{\partial z}\left[\left(\chi_h^d \rho_l \phi_l + \frac{1}{1+\Gamma}\rho_g \phi_g\right)v + \frac{1}{1+\Gamma}\rho_g \phi_g(v_g - v)\right] = -\frac{2\rho_g \phi_g u_g}{R(1+\Gamma)} \qquad (4)$$

$$\frac{\partial}{\partial t}\left(\chi_c^d \rho_l \phi_l + \frac{\Gamma}{1+\Gamma}\rho_g \phi_g\right) + \frac{\partial}{\partial z}\left[\left(\chi_c^d \rho_l \phi_l + \frac{\Gamma}{1+\Gamma}\rho_g \phi_g\right)v + \frac{\Gamma}{1+\Gamma}\rho_g \phi_g(v_g - v)\right] = -\frac{2\Gamma\rho_g \phi_g u_g}{R(1+\Gamma)} \qquad (5)$$

(e.g., Kozono & Koyaguchi, 2012; Schneider et al., 2012). In these equations, subscripts s, l, g, h, and c denote solids, liquid melt, gas, water, and carbon dioxide, respectively. The density of each phase is ρ, while ϕ is the volume fraction, and χ^d is the mass fraction of dissolved volatiles in the melt. The ratio of exsolved carbon dioxide to exsolved water is denoted by $\Gamma = \chi_c^e/\chi_h^e$, where the superscript e represents exsolved volatiles and is uniquely determined by the mole fraction of water in the vapor phase (section 2.3). Vertical and lateral gas velocities are represented by v_g and u_g, respectively. At steady state, the first term of each equation, which represents time-dependent change in mass of each component, is identically 0.

Equation (3) considers both crystals and melt together. Since crystals are formed from the melt, any decrease in melt volume fraction is balanced by an increase in solid volume fraction. Equations (4) and (5) refer to the mass balance of water, the dominant volatile species, and carbon dioxide, respectively. The first depth-dependent term in these two equations represents flux gradients of dissolved and exsolved volatiles, determined using the solubility relation of Liu et al. (2005). The second depth-dependent term represents vertical gas flow through the magma. Both equations have a nonzero sink term representing lateral gas loss (e.g., Schneider et al., 2012). Expressions for gas velocities are discussed in section 2.3.

2.2. Crystallization in the Conduit

In contrast to Anderson and Segall (2011) who specified a depth of crystallization, we allow magma to solidify gradually during ascent assuming equilibrium crystallization at a specified temperature. We employ the equilibrium crystallization model of Schneider et al. (2012), based on the MELTS thermodynamic model (Ghiorso & Sack, 1995) with the water-saturated Mount St. Helens dacite chemical composition of Pallister et al. (2008). This approach neglects the kinetics of crystallization since the ascent rate during the 2004–2008 Mount St. Helens eruption was sufficiently slow. The solid mass fraction relative to nonvapor phases (ratio of mass of solids to combined mass of solids and melt) increases as magma depressurizes at a given temperature (Figure 2a). We translate specific curves for the Mount St. Helens dacite composition to a lookup table to estimate solid mass fraction at each depth for a given temperature. The nonvapor phase solid mass fraction χ_s^{nv} is related to the total solid volume fraction ϕ_s through

$$\phi_s = \chi_s^{nv}\frac{\rho - \rho_g \phi_g}{\rho_s}. \qquad (6)$$

Bulk density is the mixture density of the solid, melt, gas, and dissolved volatile phases, first expressed as a sum of component densities and their respective volume fractions and second in terms of the mass fraction of dissolved volatiles (mass ratio of dissolved volatiles to combination of dissolved volatiles and melt),

$$\rho = \rho_s \phi_s + \rho_l \phi_l + \rho_g \phi_g + \rho_h^d \phi_h^d + \rho_c^d \phi_c^d$$
$$= \rho_s \phi_s + \rho_l \phi_l \left[1 + \chi_h^d + \chi_c^d \right] + \rho_g \phi_g, \tag{7}$$

where the solid and liquid densities ρ_s, ρ_l are prescribed and ρ_g is calculated assuming the ideal gas law.

Conduit models typically express the bulk viscosity of the magma as

$$\eta = \eta_m(\chi_h^d, \chi_c^d, T) \, \eta_s(\phi_s, \dot{\gamma}) \, \eta_b(\phi_g, Ca) \tag{8}$$

(Costa et al., 2007; Mader et al., 2013; Melnik & Sparks, 2002), where η_m is the melt viscosity, η_s is the viscosity increase due to solids, and η_b is the relative viscosity due to gas volume fraction ϕ_g and capillary number Ca (Llewellin & Manga, 2005). In this work, we use the dacitic melt viscosity model of Whittington et al. (2009) which depends on dissolved volatile content and temperature, and model viscosity increase due to solids following Costa (2005), which was based on experimental data from Lejeune and Richet (1995). Using a larger experimental data set, Caricchi et al. (2007) offered empirical equations to relate the fitting parameters of this relative viscosity model to strain rate $\dot{\gamma}$. Finally, we assume $\eta_b = 1$ because porosity of the 2005 Mount St. Helens dome lavas is relatively low. We expect the effect of bubbles on viscosity to be negligible relative to the effect of crystals (Llewellin & Manga, 2005).

2.3. Solubility and Gas Escape From the Conduit

As in Anderson and Segall (2011), the dissolved water and carbon dioxide concentrations χ_h^d and χ_c^d are determined using the solubility relations in Liu et al. (2005), which can be condensed into the following form involving the mole fractions of water m_h and carbon dioxide m_c,

$$\chi_h^d = S_h(p, T, m_h, m_c)$$
$$\chi_c^d = S_c(p, T, m_h, m_c). \tag{9}$$

Note that the mole fractions of the two volatile phases sum to unity, $m_h + m_c = 1$, which eliminates m_c as an independent variable in the above equations. The exsolved mass fractions are given by the difference between the total volatile concentration and the dissolved concentration determined from (9), for example, $\chi_h^e = \chi_h - \chi_h^d$. Finally, the molar and mass concentrations are related by

$$\chi_c^e = \frac{\chi_h^e}{B} \frac{m_c}{m_h} = \frac{\chi_h^e}{B} \frac{1 - m_h}{m_h} \equiv \Gamma \chi_h^e, \tag{10}$$

where B is the ratio of the molecular mass of water to carbon dioxide. Equation (10) serves to define Γ in equations (4) and (5).

Gas loss is modeled with Darcy's Law assuming that the gas phase is in both chemical and mechanical equilibrium with the ambient melt. This requires that the decompression timescale τ_{dec} is long relative to the timescale of volatile diffusion through the melt τ_{diff} (Gonnermann & Manga, 2013). For the 2004–2008 eruption at Mount St. Helens, $\tau_{\text{dec}} = L/v \sim 3{,}500\,\text{m}/(10^{-5}\,\text{m/s}) \sim 10^8\,\text{s} \approx 3\,\text{years}$ (Major et al., 2008). Taking τ_{dec} to be an order of magnitude longer than the diffusion timescale $\tau_{\text{diff}} = d_b^2/D$, where d_b is the bubble separation and $D \sim 10^{-10}\,\text{m}^2/\text{s}$ is the volatile diffusivity (Behrens et al., 2004), and solving for d_b, we obtain $d_b = \sqrt{0.1\tau_{\text{dec}}D} \sim 10^{-1.5} = 0.03\,\text{m}$, which is large compared to the vesicle spacing in rock samples from the eruption. A smaller d_b would give a smaller τ_{diff}, so τ_{dec} is justified to be comparatively long, which supports the assumption of chemical equilibrium between the vapor phase and dissolved volatiles. Additionally, we assume that bubble expansion through the viscous fluid is fast relative to the decompression time, $\tau_{\text{visc}} = \eta/(p_{\text{gas}} - p) \ll \tau_{\text{dec}}$ (Gonnermann & Manga, 2013). At 850°C and a low dissolved water content of 1 wt %, the Whittington et al. (2009) dacite melt model predicts a viscosity of $\sim 10^6\,\text{Pa s}$. Assuming that $\tau_{\text{visc}} < 0.1\tau_{\text{dec}}$ limits bubble overpressures to $p_{\text{gas}} - p \simeq 10^{-1}\,\text{Pa}$ before expansion occurs. This very small pressure difference indicates that we can assume that the bubble growth will not be limited by viscous resistance.

Laterally, gas flows through both magma and wall rock. We employ a "membrane diffusion" approximation and take the lateral pressure gradient to be the difference between the magma pressure p and the far-field hydrostatic pressure p_{hyd} over a length scale for percolation λ (Jaupart & Allègre, 1991; Kozono & Koyaguchi, 2012; Schneider et al., 2012). The pressure gradient for vertical Darcy flow is the magma pressure gradient $\partial p / \partial z$, where, following from the above arguments, we assume that pressures in the gas and magma are equal. Lateral and vertical gas velocities are therefore given by

$$u_g = \frac{k_{lat}}{\eta_g} \frac{p - p_{hyd}}{\lambda}$$
$$v_g = v + \frac{k_{mag}}{\eta_g} \frac{\partial p}{\partial z}. \tag{11}$$

Magma permeability is based on a Carman-Kozeny relation,

$$k_{mag} = k_c \phi_g^3, \phi_g > \phi_{gc} \tag{12}$$

where k_c is a scaling constant and ϕ_{gc} is the percolation threshold, the minimum porosity to form interconnected pathways (Blower, 2001; Klug & Cashman, 1996; Saar & Manga, 1999). As magma ascends and gases exsolve, the gas volume fraction increases until it meets the percolation threshold and magma transitions from zero to finite permeability. The lateral permeability k_{lat} includes contributions from the magma and wall rock. We apply the average crustal permeability model of Manning and Ingebritsen (1999) for the wall rock permeability and combine the two permeabilities using a harmonic average assuming $\lambda > R$,

$$\frac{\lambda}{k_{lat}} = \frac{R}{k_{mag}} + \frac{\lambda - R}{k_{wall}}. \tag{13}$$

For simplicity, we chose $\lambda = 2R$ so that magma and wall rocks contribute equally to the lateral permeability. Increasing λ would increase the contribution from the wall rocks.

We include two modifications to the above permeability model. First, we consider hysteresis in magma permeability. During bubble expansion, permeability at a specified porosity is found to be lower than during bubble collapse (Rust & Cashman, 2004). Once interconnected pathways have formed, they continue to remain open, albeit narrowed, if the gas volume fraction subsequently decreases. We implement hysteretic permeability in a simple way: after the percolation threshold is met, equation (12) applies for all ϕ_g. Although more complicated models for hysteretic permeability exist (e.g., Michaut et al., 2009), not enough is known about their parameters for use in this study.

The second modification addresses the possibility of gas overpressure at shallow depth. Due to volatile exsolution and crystallization, viscosity increases and bubble expansion becomes severely limited by viscous resistance (Gonnermann & Manga, 2007). Either overpressure must develop, or as the magma becomes largely solid, sufficient gas must escape to release this overpressure. Here we assume the latter. Once the plug is formed, we no longer evaluate equations (12) and (13) but rather assume that the magma is sufficiently permeable that enough gas is lost to keep the gas pressure in equilibrium with the melt phase without bubble expansion (i.e., porosity is constant). We refer to this modification as "plug gas loss". Without it, porosity continues to increase as pressure decreases and generally reaches a fragmentation condition.

2.4. Numerical Solution of Forward Model

The governing equations consist of momentum balance plus the steady state form of equations (3)–(5), which can be written as a system of implicit first-order ordinary differential equations (ODEs). Table 1 lists and classifies the symbols. Conduit radius R; and friction parameters v_r, f_0, a are assumed independent of depth and prescribed in the forward model but estimated in the inversion. Normal stress on the conduit walls is expressed as a function of depth. Magma properties such as density and viscosity depend on the volume fraction and component density of each phase as described in section 2.2, while solubility depends on pressure and mole fraction of water as in (9), and gas escape follows (11). Independent system parameters are either prescribed if they have been previously estimated or later constrained in the Bayesian inversion.

This leaves four remaining field variables to be solved in the governing equations, compiled into the vector $y(z) = [p, v, \phi_g, m_h]$. Discretizing the steady state system of equations into N elements in z, each of the

governing equations represents $N-1$ equations, giving a total of $4(N-1)$ equations. Since $y(z)$ for $[z_1, \dots, z_N]$ contains $4N$ variables, four boundary conditions are required to close the system: pressure at the conduit top (atmospheric pressure), pressure at the conduit base p_{ch}, and total water and carbon dioxide concentrations (χ_h^{ch}, χ_c^{ch}) at the conduit base. Here the superscript ch refers to the magma chamber. We do not consider the back pressure exerted by the dome here, but this could be included simply by adjusting the pressure boundary condition at the conduit top. Since the governing equations do not explicitly depend on the total volatile concentrations, we require two equations to relate χ_h^{ch} and χ_c^{ch} to ϕ_g^{ch} and m_h^{ch}. First, m_h^{ch} can be found by computing the exsolved mass fractions as the difference between total and dissolved mass fractions, then eliminating χ_h^e,

$$\Gamma^{ch}[\chi_h^{ch} - S_h(p_{ch}, T, m_h^{ch})] = [\chi_c^{ch} - S_c(p_{ch}, T, m_h^{ch})]. \tag{14}$$

For given $p_{ch}, T, \chi_h^{ch}, \chi_c^{ch}$, this represents an implicit expression for m_h^{ch}. We then obtain ϕ_g^{ch} from the definition of volatile mass fractions,

$$\chi_h^{e,ch} + \chi_c^{e,ch} = \chi_h^{ch} - S_h(p_{ch}, T, m_h^{ch}) + \chi_c^{ch} - S_c(p_{ch}, T, m_h^{ch}) = \left[\frac{\rho_g \phi_g}{\rho_l \phi_l (1 + \chi_h^d + \chi_c^d)} \right]_{ch}. \tag{15}$$

The above two equations only apply in the chamber and suffice to close the system of equations. For the remainder of the conduit, we solve directly for m_h and ϕ_g.

As described in more detail in Appendix A, the momentum balance (1) is solved for the pressure gradient dp/dz. Together with the continuity equations ((3)–(5)), this forms an implicit system of ODEs, which is solved using the shooting method as follows. Given boundary conditions at the conduit base and an estimate of the conduit base velocity v_{ch}, the system of equations is integrated to the surface. The estimate of v_{ch} is adjusted until the difference between predicted surface pressure and atmospheric pressure is approximately equal to zero within the prescribed tolerance. Note that the final solution may contain discontinuous derivatives caused by, first, the transition from zero to finite permeability at the percolation threshold, and, second, fixed porosity once the plug is formed.

3. Forward Model Simulation Results

We first discuss results from forward model simulations which explore model parameter values as they apply to the 2005 quasi steady state eruption phase of Mount St. Helens (Table 2, more details in Appendix C1). The forward model requires specification of three boundary conditions in addition to atmospheric pressure at the surface, as well as poorly constrained material and geometric parameters: pressure p_{ch} and total water and CO_2 content, χ_h^{ch}, χ_c^{ch} at the conduit base, which serve as boundary conditions, the permeability scaling constant k_c, and percolation threshold ϕ_{gc}, which determine the magma permeability, the nominal friction coefficient f_0 and rate dependence of friction a, and the conduit radius R. Total CO_2 content cannot be constrained without gas measurements, so we fix this to 2,000 ppm, an approximation derived by applying the 37 ppm dissolved CO_2 from Gerlach et al. (2008) in the Liu et al. (2005) solubility model at 85 MPa with 4.5 wt % total water. The remaining parameters comprise the model vector $\mathbf{m} = [p_{ch}, \chi_h^{ch}, k_c, \phi_{gc}, f_0, a, R]$. Other independent system parameters are prescribed beforehand.

To compare forward model results with the Mount St. Helens eruption, we use data from (1) porosity of extruded lava, (2) spine exit velocity, (3) spine exit volume flux, (4) depth of transition from viscous flow to plug flow (plug depth), and (5) solidus depth. Plug depth is inferred from the depth of "drumbeat earthquakes" (Iverson et al., 2006), while the solidus depth is constrained through the groundmass crystallization pressure (Cashman et al., 2008). Data ranges are listed in Table 2 with more detail of their selection in Appendix C2. We use these data to constrain the Bayesian inversion (section 4).

3.1. Model Uniqueness
To analyze uniqueness in the forward model, we determine whether a given set of model parameters permits multiple solutions that satisfy atmospheric pressure at the surface. Uniqueness is achieved when only one conduit base velocity v_{ch} yields a solution that matches this surface condition.

Extensive searching of the model space reveals that most choices of model parameters produce unique solutions; however, in some extreme cases, solutions are nonunique. The difference between surface pressure

Table 2

Range of Model Parameter Values and Data Used in Forward Model Analysis, Also Applied as Bounds on the Uniform Part of the Prior and Data in Bayesian Inversion for the Steady State Phase of the Mount St. Helens Eruption (March–December 2005)

Quantity	Bounds on uniform part	Reference
Model parameter priors		
Pressure of magma chamber, p_{ch}	$75-100$ MPa	Anderson and Segall (2013)
Total water content in magma chamber, χ_h^{ch}	$3-7$ wt %	Rutherford and Devine (2008); Gerlach et al. (2008)
Magma permeability scale, k_c	$10^{-15}-10^{-5}$ m^2	Kozono and Koyaguchi (2012)
Percolation threshold ϕ_{gc}	$0.2-0.4$	Blower (2001)
Nominal coefficient of friction f_0	$0.01-0.6$	Moore et al. (2008)
Rate dependence of friction a	$10^{-2.2}-10^{-1.8}$	Rice et al. (2001)
Conduit radius R	$50-200$ m	Anderson and Segall (2013)
Eruption data		
Porosity of extruded lavas	$5-10\%$	Cashman et al. (2008); Smith et al. (2011)
Spine exit velocity	$3-7 \times 10^{-5}$ m/s	Major et al. (2008); Vallance et al. (2008)
Spine exit volume flux	$1-2$ m^3/s	Schilling et al. (2008)
Plug formation depth	$0.5-1.5$ km	Iverson et al. (2006); Thelen et al. (2008)
Solidus depth	$0.5-1.5$ km	Cashman et al. (2008); Pallister et al. (2008)

Note. In the inversion, Gaussian tails with standard deviation equal to 10% of the width of the uniform part are applied to extend these bounds.

predicted by a wide range of v_{ch} and atmospheric pressure is shown for five model parameter sets in Figure 3. All models except A cross 0 exactly once. Model A shows that nonuniqueness is possible when chamber pressure and magma permeability are low—in this case there are four solutions. The physical basis for nonuniqueness has been identified in previous work (Kozono & Koyaguchi, 2012; Melnik & Sparks, 2005). At low v_{ch}, the timescale of magma ascent is long, allowing more time for gas to escape through the walls, reducing exsolved gas content within the conduit. Magma density consequently increases, offering more resistance to flow. Conversely, at high v_{ch}, gas content in the conduit remains high, decreasing density and allowing magma velocity to remain relatively high. Although we include this nonunique region of the model space in subsequent analyses, we find that the Bayesian inversion for Mount St. Helens rejects these model parameter combinations, thus avoiding nonunique inversion results (section 5). When applying data from other eruptions, one should be careful and investigate the effect of nonunique forward model solutions on inversion results as this effect will be problem specific.

Increasing the conduit base pressure (Model C) translates the curve to higher surface pressures so that only the root corresponding to the higher v_{ch} model exists. Increasing magma permeability (Models B, D, and E) reduces the height of the peaks and shifts them to lower v_{ch}. Gas escape occurs with greater ease (equation (11)), increasing magma density. The prescribed chamber pressure can only extrude the heavier magma column at a lower speed.

3.2. Overview of Model Behavior

We solve the forward model to obtain depth-dependent conduit properties using representative values for Mount St. Helens (Figure 4). The percolation threshold of 0.30 is met at ∼ 1.3 km depth, and gas transport commences. At this depth, the magma permeability is high (Figure 4f), allowing vertical gas escape to dominate, while lateral gas flow is limited by the wall rock permeability. As gas is lost, the magma permeability decreases to the wall rock permeability so that both lateral and vertical permeability are comparable. Gas escape causes the gas volume fraction to decrease, which results in a corresponding increase in density and decrease in velocity (Figure 4d).
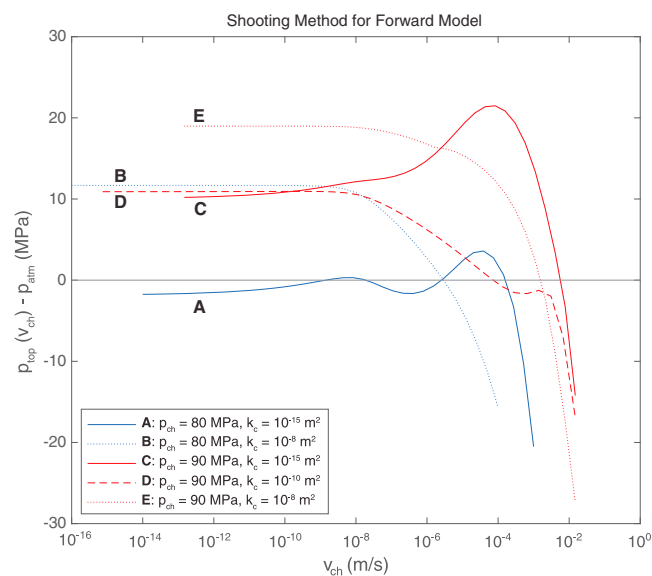

Figure 3. Exploration of model uniqueness for parameter values $\chi_h^{ch} = 5$ wt %, $\phi_{gc} = 0.2, f_0 = 0.08, a = 0.01, R = 100$ m, while p_{ch} and k_c are varied. Chamber exit velocity v_{ch} is tested systematically to obtain pressure at the top of the conduit p_{top} for each parameter set. A solution is found when $p_{top} - p_{atm} = 0$. Model A shows multiple zero crossings, indicating that solutions are nonunique. All other models shown here produce unique solutions.
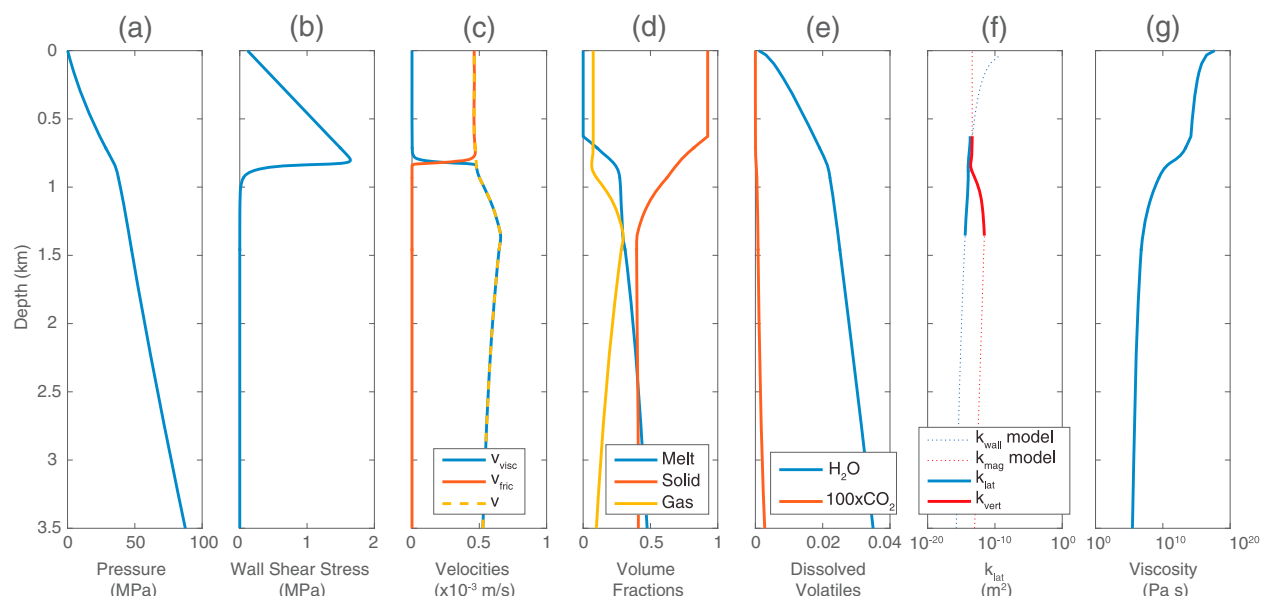
Figure 4. Key properties for forward model with nominal parameter values for Mount St. Helens. At the bottom of the conduit, pressure is 87.5 MPa and total water content is 5.0 wt %. The permeability scaling constant is 10^{-10} m^2, and the percolation threshold is 0.3. The nominal coefficient of friction is $f_0 = 0.088$, and conduit radius is 100 m. Magma and wall permeability are shown as solid lines where permeability is active and "plug gas loss" is not.

The plug depth is at ~0.8 km, where magma flow switches abruptly from viscous flow to frictional sliding (Figure 4c). Pressure decreases at a relatively steady rate until this depth, above which it begins to decrease more rapidly. This change in pressure gradient corresponds to the peak in shear stress along the conduit wall (Figure 4b). The solid fraction increases rapidly and reaches a maximum value at the solidus depth of ~0.6 km, while the melt and gas fractions decrease to their minimum. These phase changes cause the magma viscosity to increase rapidly (Figure 4g), contributing to the rheological transition to plug flow (Figure 4c).

To capture the overall flow dynamics, multiple forward models are evaluated to examine the relationship between mass flux and chamber pressure, and to offer comparison with other studies (e.g., Kozono and Koyaguchi, 2012). Changing the wall rock permeability (for fixed k_c) causes the mass flux to vary between the efficient gas escape curve and the no lateral gas escape curve. On the other hand, changing k_c (for fixed k_w) causes the mass flux to vary between efficient and no gas escape, since magma permeability factors into both
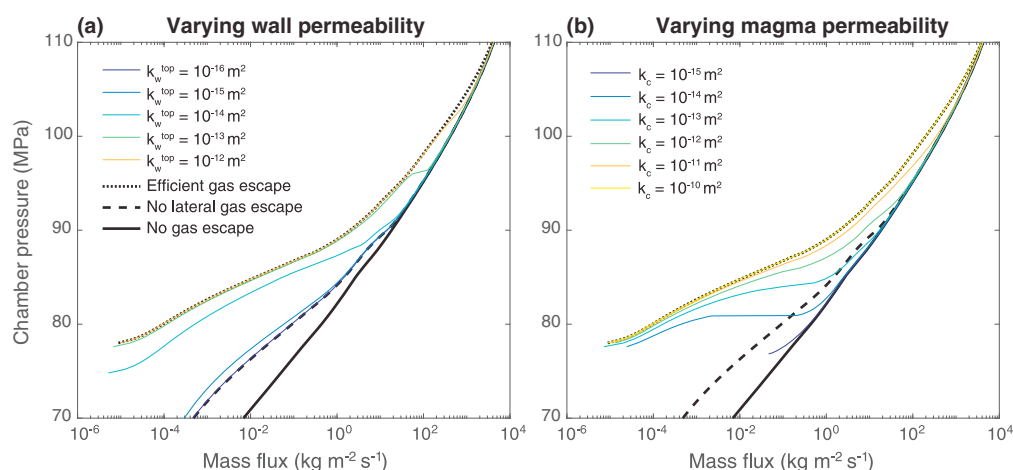

Figure 5. Effect of changing permeability properties on the mass flux of the system for models with $\chi_h^{ch} = 5$ wt %, $\phi_{gc} = 0.3$, $R = 100$ m, $a = 0.01$, and $f_0 = 0.088$. The limiting cases shown in black lines are defined as in Kozono and Koyaguchi (2012). (a) The effect of varying k_{wall}^{top} while keeping $k_c = 10^{-10}$ m^2. (b) The effect of varying k_c while keeping $k_{wall}^{top} = 10^{-12}$ m^2.
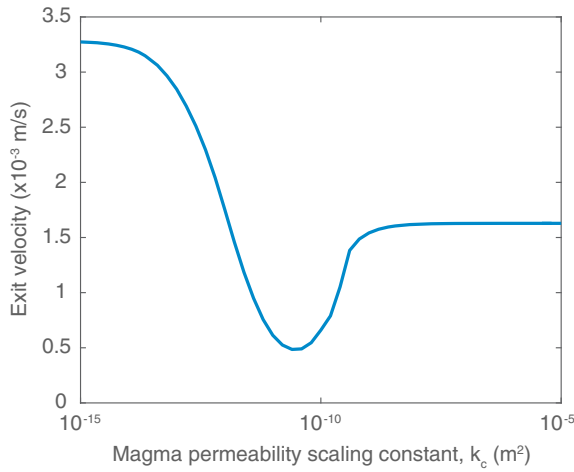
Figure 6. Sensitivity of exit velocity to the magma permeability scaling constant k_c. As k_c increases from 10^{-15} m^2, exit velocity decreases and reaches a minimum at $k_c \approx 10^{-10}$ m^2, after which it increases.

lateral and vertical gas transport. In some cases, the flux exhibits a jump that indicates a crossover from the low to high flux models. This crossover is most noticeable for $k_{wall}^{top} = 10^{-13}$ m^2 at ~ 95 MPa in Figure 5a and for $k_c = 10^{-14}$ m^2 and 10^{-13} m^2 in Figure 5b. As discussed in section 3.3, rapid changes occur when the magma velocity is high enough to limit gas escape, and the retained gas decreases the bulk magma density feeding back to further increase ascent velocity (Kozono & Koyaguchi, 2012).

Sensitivity tests investigated the dependence of observed data on a range of model parameter values (Appendix B). Most model parameters follow the expected behavior, such as increasing chamber pressure or water content leading to higher exit velocities. In some cases, exit velocity and porosity are inconsistent with effusive eruptive behavior and therefore represent nonphysical solutions of the governing equations, but these variations still provide insight into the forward model. Most notably, varying the magma permeability scaling constant k_c resulted in nonmonotonic changes in the predicted data (Figure 6). We explore this unexpected behavior in the next section.

3.3. Effect of Gas Escape on Conduit Flow

To understand the role of gas escape, we solved the forward model for a range of magma permeability scaling constants k_c. One expects a larger k_c to decrease porosity and exit velocity, since higher permeability permits more efficient gas escape, reducing the magma density, which should decrease velocity. This does occur initially (Figure 6); however, the velocity exhibits a minimum at $k_c \approx 10^{-10}$ m^2, after which it increases.

Examining the evolution of conduit gas content explains this nonmonotonic behavior. As magma ascends and depressurizes, volatiles exsolve and magma porosity increases. Once the percolation threshold is met, permeability becomes nonzero. Figure 7 shows gas velocities as a function of k_{mag}/k_{wall} at the percolation threshold depth, where $k_{mag} = k_c \phi_{gc}^3$. This marks a crucial transition that controls the evolution of magma porosity above this depth. Vertical gas velocity increases proportionally with k_{mag}/k_{wall} since it is independent of k_{wall}. Lateral gas velocity increases until $k_{mag}/k_{wall} \simeq 1$, after which it remains constant. Lateral permeability combines magma and wall rock permeability (equation (13)), with equal weights when $\lambda = 2R$; thus, when k_{mag} is sufficiently large, flow is limited only by the wall rock, that is, $k_{lat} \approx k_{wall}$ for $k_{mag}/k_{wall} > 1$. Chamber pressure also affects the gas velocity: higher chamber pressure increases both the vertical and lateral pressure gradients $\partial p/\partial z$ and $(p - p_{hyd})/\lambda$; thus, the respective gas velocities are also higher.
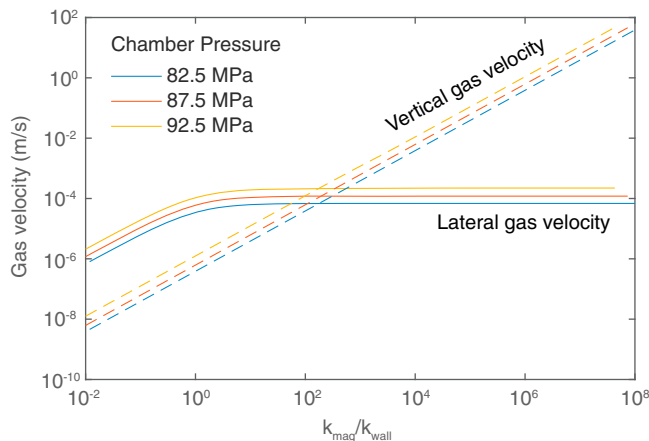

Figure 7. Gas velocities for three chamber pressures, plotted as functions of k_{mag}/k_{wall} at the percolation threshold depth for $\phi_{gc} = 0.3$. Solid lines show horizontal gas velocity u_g, which is limited by wall rock permeability ($k_{wall}^{top} = 10^{-14}$ m^2; at this depth, $k_{wall} \simeq 10^{-15}$ m^2). Dashed lines indicate differential vertical gas velocity ($v_g - v$).

Including both lateral and vertical gas flow allows us to study the competing effects between these two processes during magma ascent (Figure 8). Consider the relative timescales of lateral $t_{lat} = R/u_g$ and vertical gas flow $t_{vert} = L/(v_g - v)$, in comparison to the magma ascent timescale $t_{ascent} = L/v$. In each case, the relevant velocity is measured at the depth at which percolation threshold is met. At the low permeability extreme, lateral gas flow is negligible such that $t_{lat} \gg t_{ascent}$ (Figure 8a); t_{lat}/t_{vert} is less than 1, so vertical gas flow is also limited (Figure 8b). As magma permeability increases, lateral gas escape becomes more important and t_{lat}/t_{ascent} decreases. For lower chamber pressure models, both t_{lat} and t_{ascent} are longer, but the second effect is more pronounced, resulting in the smaller t_{lat}/t_{ascent}.

The 92.5 MPa model is monotonic with t_{lat}/t_{ascent} decreasing with increasing k_{mag}/k_{wall}; however, the other two models exhibit minima. In addition, the 82.5 MPa model shows a rapid drop when $k_{mag}/k_{wall} \sim 1$, which corresponds to $k_c \sim 10^{-13}$ m^2. This rapid drop coincides with the jump in mass flux with k_c seen in Figure 5b. Increasing the magma permeability in this region causes a sharp decrease in mass flux, such that t_{ascent} increases and causes a rapid drop in t_{lat}/t_{ascent}. At higher chamber pressures, the flux is
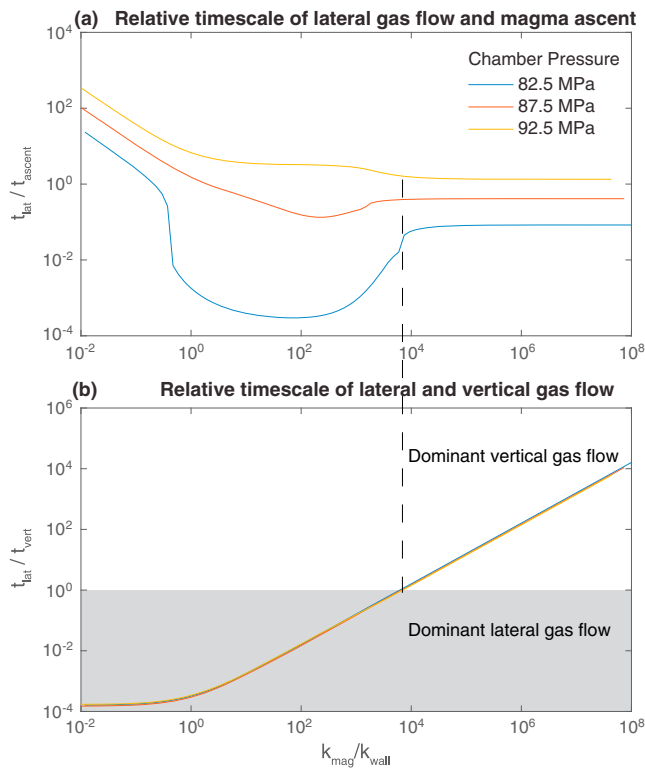
Figure 8. Relative timescales for gas flow in the system for three chamber pressures. (a) Lateral gas flow compared to magma ascent timescales. When $t_{lat}/t_{ascent} < 1$, gas escape is efficient. (b) Lateral and vertical gas flow timescales compared.

Figure 9. Exit velocity as a function of k_{mag}/k_{wall}, for different wall rock permeabilities. At extremely low wall rock permeability, monotonic trends are observed as magma permeability is the only control on gas escape. Intermediate values allow competition between lateral and vertical gas escape to produce nonmonotonic behavior. The yellow curve ($k_{wall}^{top} = 10^{-14}$) is the model from Manning and Ingebritsen (1999) used in all other calculations in this study.

less sensitive to changes in k_c. Eventually, around $k_{mag}/k_{wall} \sim 10^4$, vertical gas loss dominates lateral gas loss due to the limiting effect of wall rock permeability, and t_{lat}/t_{ascent} increases.

When gas transport is dominated by vertical flow, flow velocity and porosity are higher, because vertical transport is less efficient than lateral transport in removing gas from the magma column. This effect lowers the bulk density and increases the flow velocity. The nonmonotonic behavior in the predicted data is thus caused by the competition between lateral and vertical gas escape.

Changing the wall rock permeability alters exit velocity since it affects the relative contributions of lateral and vertical gas flow (Figure 9). Similar trends in exit velocity are observed for changing λ, where increasing λ has the same effect as lowering the wall rock permeability. For very low wall rock permeability ($k_{wall}^{top} = 10^{-16}$ m^2), lateral gas transport is negligible and gas can only escape vertically, leaving magma permeability as the only control on gas transport. In this case, we observe the expected monotonic decrease in exit velocity with increasing magma permeability. For higher wall rock permeability, we observe the nonmonotonic trend in exit velocity, beginning at $k_{mag}/k_{wall} \sim 10^2$ which is approximately the ratio of lateral to vertical pressure gradients. At a given k_{mag}/k_{wall} (e.g., 1, denoted by the dashed line), the model with the highest k_{wall}^{top} also has the highest magma permeability to maintain the same ratio of permeabilities. As a result, gas escape is very efficient and the lowest exit velocity is produced by the greatest k_{wall}^{top} model.

4. Bayesian Inversion Using Eruption Data From Mount St. Helens 2004–2008

One of the goals of this work is to apply the physics-based forward model together with observations to constrain otherwise poorly known properties of the Mount St. Helens magmatic system. The data likelihood function has multiple extrema due to the nonlinearities in the governing equations. Stochastic methods can search the parameter space comprehensively to determine locations of both local optima and, more importantly, the global optimum while also providing useful constraints on parameters (Mosegaard & Tarantola, 1995). Bayes' theorem provides a framework for quantifying model uncertainties because the results are presented as the posterior probability density function (PDF) of the model parameters **m** conditional on the data, **d**, $P(\mathbf{m} \mid \mathbf{d})$,

$$P(\mathbf{m} \mid \mathbf{d}) \propto P(\mathbf{d} \mid \mathbf{m})P(\mathbf{m}), \qquad (16)$$

where $P(\mathbf{d} \mid \mathbf{m})$ is the data likelihood function, and $P(\mathbf{m})$ is the prior distribution on the model parameters. The prior distributions encode information that we already know about the model parameters and are considered to be independent. The simplest prior is a uniform distribution between two bounds, but this approach assumes definitive bounds. To account for uncertainties in these bounds, we apply Gaussian-tailed uniform distributions (Anderson & Poland, 2016). We assign the standard deviation of the tails to be 10% of the width of the uniform part, whose bounds are given in Table 1.

The data likelihood measures the misfit between the predicted and observed data, and its distribution reflects the uncertainties in the data. In Anderson and Segall (2013), data uncertainties are taken to be Gaussian and each data set was considered independent. However, data analyzed here from the 2004–2008 eruption of Mount St. Helens are given as ranges
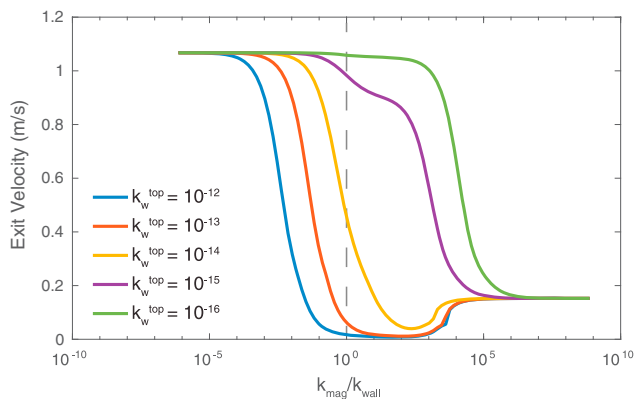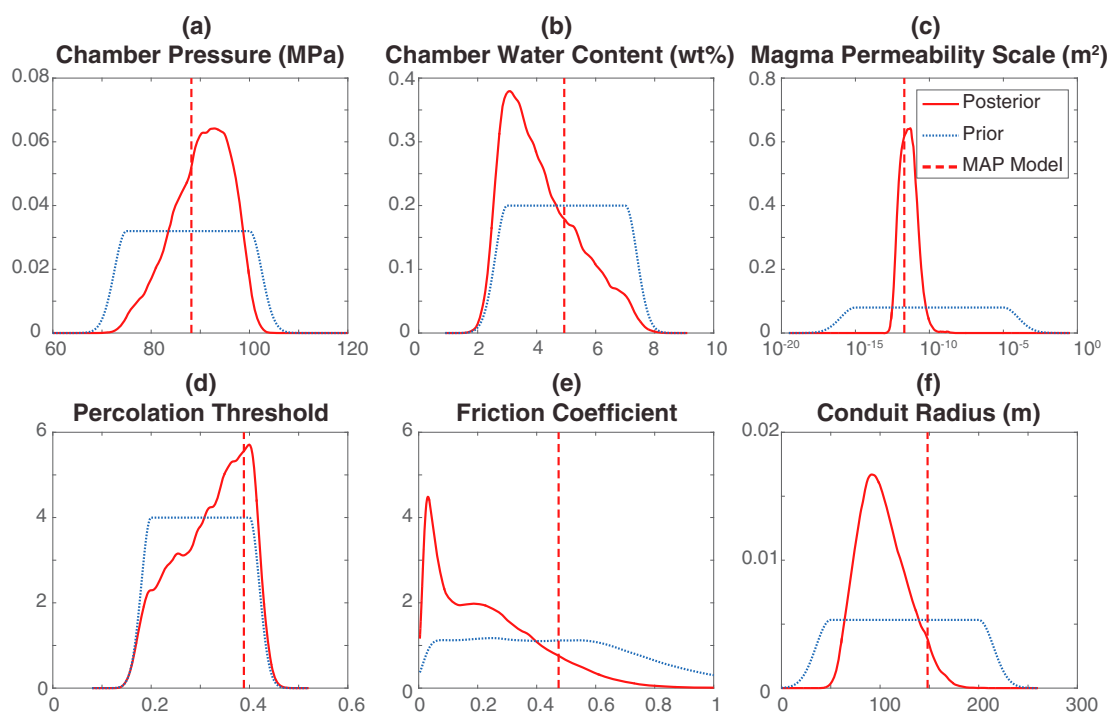
Figure 10. Posterior distributions of model parameters from the MCMC inversion with 1.25×10^6 samples. The parameter f is calculated from the PDFs of f_0 and a, measured at $v_r = 10^{-5}$ m/s, while all other parameters are directly estimated in the inversion. Dashed blue lines indicate prior distributions, while red solid lines indicate posterior distributions. The vertical dashed red line is the maximum a posteriori (MAP) model.

rather than mean values, so we implement Gaussian-tailed uniform distributions for the likelihood function as well (bounds given in Table 2). The Gaussian tails reflect uncertainties in estimating the range of values given in the literature. These bounds, as well as bounds on the prior distribution, are discussed in detail in Appendix C.

We sample the posterior PDF using a Markov Chain Monte Carlo (MCMC) algorithm with the Metropolis-Hastings criterion (Hastings, 1970; Metropolis et al., 1953). The algorithm is summarized below, and more detail can be found in Anderson and Segall (2013). Given a set of parameters **m**, we solve the forward model and compute the likelihood of observing the predicted data $P(\mathbf{d} \mid \mathbf{m})$. The posterior probability is then calculated from (16). In the next iteration, the algorithm uses a random walk to generate another candidate set of model parameters and then repeats the previous steps to find the corresponding posterior probability (e.g., Mosegaard and Tarantola, 1995). The candidate model parameters are retained in the posterior PDF according to the Metropolis-Hastings criterion. Better fitting models are always retained, while poorer fitting models are sometimes retained, depending on the ratio of the posterior probabilities at the current and former step. This process is repeated over many iterations to build the posterior PDFs of the model parameters.

5. Parameter Constraints Derived in Bayesian Inversion

Probability density functions (PDFs) of the model parameters are displayed in Figure 10, while correlations between model parameters are shown in Figure 11. Parameters of the maximum a posteriori (MAP) model are shown in Table 3 together with the mean, standard deviation, and 90% credible interval. Since the present discussion is limited to steady state behavior, the friction parameters f_0 and a have been collapsed into one parameter f measured at $v = v_r = 10^{-5}$ m/s to reduce the six-dimensional space to a five-dimensional space. Note that the PDFs of total water content and percolation threshold extend beyond the uniform part of their distributions.

Estimated magma chamber pressures tend toward the upper bound of the uniform part of the prior, with a mean and mode around 90 MPa. The standard deviation of 5.9 MPa indicates that most accepted models lie within the uniform part of the prior, and the 90% credible interval ([79.4, 98.7] MPa) shows improved constraints from the prior. These relatively high values indicate that viscous and frictional losses during magma
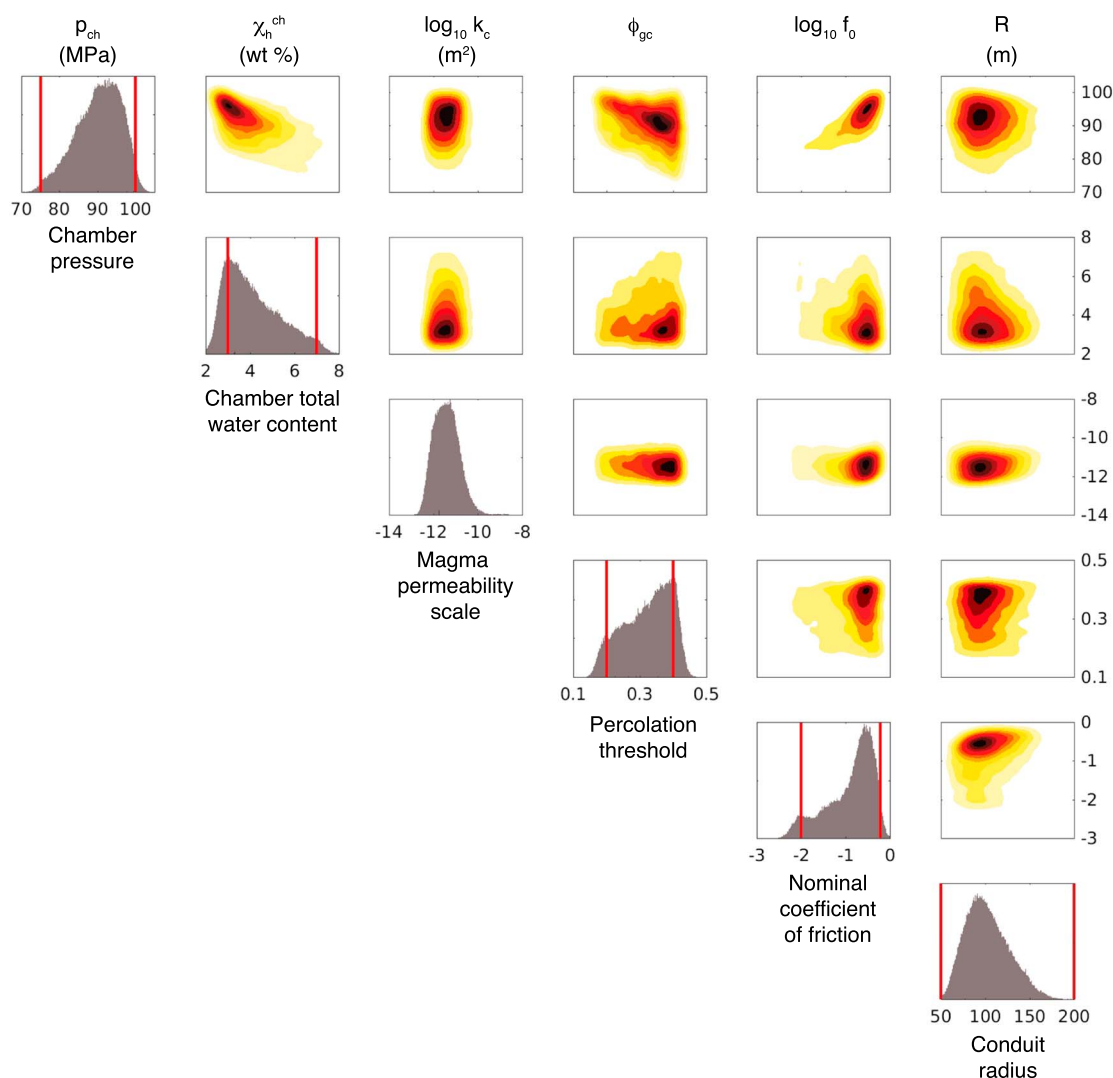
Figure 11. Correlation plots of model parameters. Note that the color scale differs for each panel. Red vertical lines denote bounds of the uniform part of the prior distribution. Chamber pressure correlates negatively with total water content and percolation threshold but positively with the coefficient of friction.

ascent are large, requiring a higher chamber pressure to extrude magma at the observed rate. A few models with chamber pressure greater than the prescribed upper bound of 100 MPa are accepted. In reality, such high pressures may produce intrusions into the surrounding crust, but this effect is not modeled here; therefore, these high-pressure models require high coefficients of friction to relieve the excess pressure. Additionally, these models produce a distribution of extrusion velocities that is skewed toward the upper bound of 7×10^{-5} m/s. At the other extreme, very few models with anomalously low chamber pressures are accepted, corresponding to models with low extrusion velocity. These models require minimal viscous and frictional losses, such that even at these low pressures, overpressure at the conduit base is sufficient to drive flow at the lower bound of the observed rate.

Total water content tends toward the lower bound of the prior, with most accepted models between 3 and 5 wt % with a mean at 4.15 wt %. The PDF captures the range obtained from analysis of amphiboles in Rutherford and Devine (2008) and gas emissions in Gerlach et al. (2008). Surprisingly, the total water content is uncorrelated with permeability or percolation threshold but is negatively correlated with chamber pressure. Since a higher water content strongly increases exit porosity and flux, lowering chamber pressure keeps the predicted data within the observed range.

The scaling constant for magma permeability is well constrained with a Gaussian-like distribution in logarithmic space centered at $10^{-11.4}$ m^2 with a narrow range described by the 90% credible interval of

Table 3
Constraints on Model Parameters From Bayesian Inversion

Quantity	MAP model	Mean	Standard deviation	90% credible interval
Pressure of magma chamber, p_{ch}	88.2 MPa	90.2 MPa	5.9 MPa	[79.4, 98.7] MPa
Total water content in magma chamber, χ_h^{ch}	4.93 wt %	4.15 wt %	1.25 wt %	[2.56, 6.61] wt %
Magma permeability scale, k_c	$10^{-11.7}$ m^2	$10^{-11.4}$ m^2	$10^{0.57}$ m^2	$[10^{-12.3}, 10^{-10.5}]$ m^2
Percolation threshold, ϕ_{gc}	0.39	0.32	0.072	[0.19, 0.42]
Nominal coefficient of friction, f_0	$10^{-0.34} = 0.46$	$10^{-0.89} = 0.13$	$10^{-0.54}$	$[10^{-2.0}, 10^{-0.25}]$
Rate dependence of friction, a	$10^{-1.94} = 0.012$	$10^{-1.96} = 0.011$	$10^{1.40}$	$[10^{-2.2}, 10^{-1.8}]$
Conduit radius, R	148 m	103 m	24 m	[67, 147] m

$[10^{-12.3}, 10^{-10.5}]$ m^2. This range of k_c represents a balance that allows the given volatile content in the magma chamber to produce the observed dome rock porosity, given the specified wall rock permeability. No models with $k_c < 10^{-13}$ m^2 were accepted; thus, the MCMC avoided the nonunique part of the model space as described in section 3.1.

The inferred percolation threshold shows a broad distribution, with the mode close to the upper bound of 0.4 which coincides with the MAP model. This range is slightly higher than but includes most experimental estimates of ~ 0.3 (Blower, 2001). No correlation between percolation threshold and permeability is observed, but there is a slight negative correlation with chamber pressure. Higher ϕ_{gc} causes more volatiles to be retained in the conduit, which increases exit porosity, velocity, and flux. These effects can be compensated by decreasing magma chamber pressure.

The conduit radius shows slightly improved constraints from the prior, with the 90% credible interval given by 67 and 147 m, respectively. The MAP model has a larger conduit radius than the mean, but this is accounted for by the relatively high coefficient of friction that regulates the magma flow rate.

Most accepted models have coefficients of friction less than 0.3 with a peak at 0.02, extremely low relative to typical rock values of 0.6 (Byerlee, 1978), and also smaller than experimental estimates of 0.42–0.47 for the Mount St. Helens fault gouge (Moore et al., 2008). Possible explanations for low nominal friction coefficients are discussed in section 6. Nevertheless, the MAP model prefers a friction coefficient of 0.46 which is consistent with experimental estimates. As expected, the coefficient of friction is positively correlated with chamber pressure and conduit radius. If chamber pressure is low, the coefficient of friction must correspondingly be low to enable magma to extrude at the observed rate, while a larger conduit radius increases the magma velocity and flux by R^2 and R^4, respectively (equations (1) and (2)); thus, a higher coefficient of friction can be accommodated. The coefficient of friction does not exhibit any obvious correlation with the other model parameters.

5.1. Maximum A Posteriori Model

One of the main advantages of the MCMC approach is that it generates PDFs of the model parameters, rather than only finding the best fit model. From the PDFs in Figure 10, we can see that the spread in the models is large and the distributions markedly non-Gaussian, so the system would not be sufficiently characterized by the maximum a posteriori (MAP) model, or the mean model and covariance. Nevertheless, the MAP model indicates which model is most consistent with prior assumptions and observations. Some properties of the MAP model are shown as functions of depth in Figure 12.

Dramatic changes occur at two depths in the shallow conduit: the percolation threshold depth and the plug formation depth. The percolation threshold marks when permeability becomes active, at ~0.8 km depth. The percolation threshold in the MAP model is 0.38, which is relatively high compared to experimental estimates (Blower, 2001; Klug & Cashman, 1996; Saar & Manga, 1999), although smaller values are also consistent with the data in Figure 10. As magma rises from the chamber, the gas volume fraction increases until it exceeds the threshold at ~0.8 km. At this depth, gas escapes so that solids and liquids take up larger volume fractions (Figure 12d). The flow velocity decreases at this depth as the magma density increases (Figure 12c). Since permeability is hysteretic, gas transport persists at shallow depth even though the porosity drops below the percolation threshold.
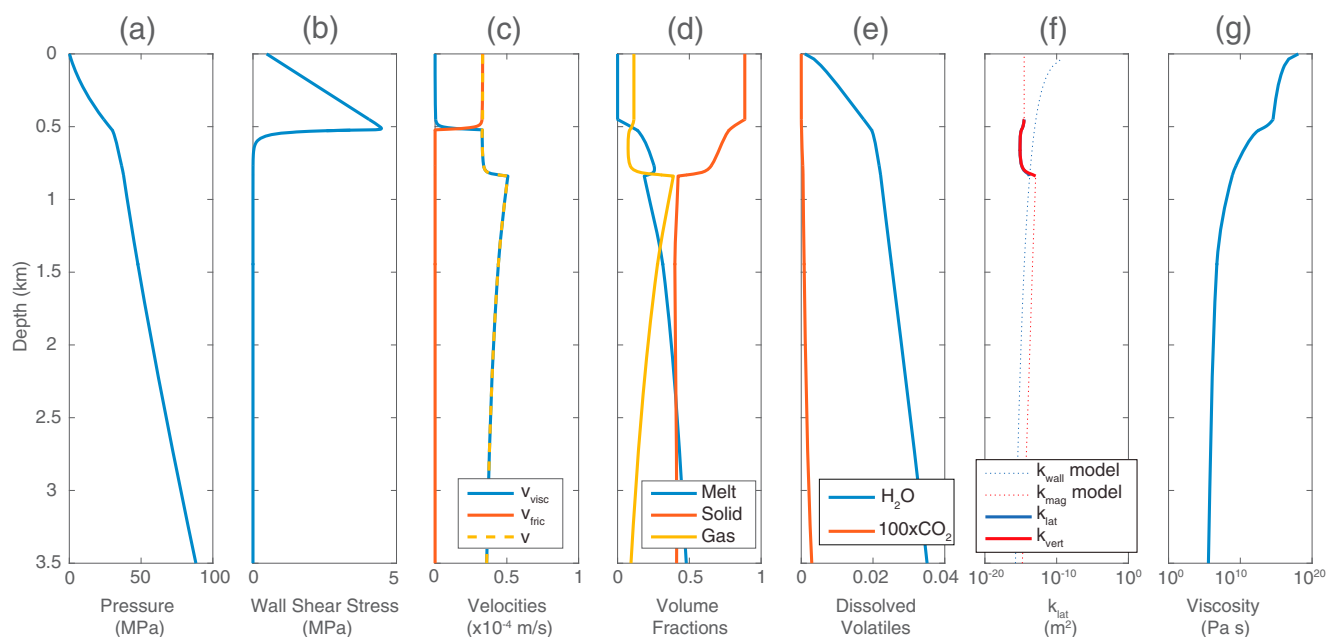
Figure 12. Key properties plotted for the maximum a posteriori model obtained from MCMC inversion. Sharp changes occur at the percolation threshold depth at ∼0.8 km and plug depth at 0.5 km. Magma and wall permeability are shown in solid where permeability is active and "plug gas loss" is not.

Viscosity increases exponentially as depth decreases, leading to a rheological transition to plug flow at ∼ 0.5 km depth, where the viscous and frictional velocities trade off over a narrow depth range (Figures 12c and 12g). This depth also corresponds to a peak in shear stress. Between the percolation threshold and the plug transition, the volume fraction of solid increases dramatically so that very little melt phase is present. The remaining melt solidifies at a slightly shallower depth.

6. Discussion

6.1. Implications for Mount St. Helens Eruption (2004–2008) and Future Conduit Models

The forward model developed here is specialized for effusive eruptions such as in the dome-forming eruption of Mount St. Helens from 2004 to 2008. We have shown that the governing equations create feedbacks that cause the forward model to be very sensitive to the model parameters. Small changes in parameter values (e.g., changing permeability) may lead to radically different eruption characteristics and could cause a volcano to transition from effusive to explosive behavior, although the fragmentation process in explosive eruptions is not modeled here.

Gas escape is clearly an important process that affects extrusion behavior. Mass flux can vary by orders of magnitude depending on the efficiency of gas escape (Figure 5). This result is consistent with Feedback 2 identified in Kozono and Koyaguchi (2012), as well as studies of lateral gas escape in Schneider et al. (2012). In addition, examining both lateral and vertical gas loss is critical to understanding their effect on magma velocity because they can have opposite effects on magma porosity. If we consider only vertical gas transport, the steady state continuity equation becomes

$$\frac{\partial}{\partial z}\left[\chi_h^d \rho_l \phi_l v + \frac{1}{1+\Gamma}\rho_g \phi_g v_g\right] = 0;$$ (17)

thus, the sum of the two terms in parentheses must be a constant at all depths. During ascent, solubility of water decreases, causing χ_h^d to drop. Magma is also solidifying, reducing ϕ_l. Assuming a constant Γ, this means that $\phi_g v_g$ must increase by a large amount to compensate for both the decrease in the first term and the decrease of ρ_g with pressure. If v_g is not greatly different from v, this would in fact lead to an increase in porosity. As such, while lateral gas transport always removes gas from the conduit and reduces porosity, vertical gas transport may lead to either an increase or decrease in porosity depending on k_{mag} which influences the differential vertical gas velocity ($v_g - v$).

The physics-based forward model allows us to constrain a diverse set of parameters for the Mount St. Helens 2004–2008 eruption by Bayesian inversion. We find magma chamber water contents that agree with the inversion results of Anderson and Segall (2013). Even with the addition of gas loss, the inversion continues to prefer relatively low chamber water contents, consistent with the eruption style. We suggest that modeling gas escape provides physical constraints on water content in addition to petrologic data. Simply through the balance of volatile content at the base of the conduit with the observed porosity at the surface, we have also obtained physical constraints on the magma permeability given a prescribed wall rock permeability model.

Additionally, we obtain improved constraints on physical properties of the conduit system. First, we derive higher chamber overpressures than estimated in Anderson and Segall (2013). Overpressure is defined here as the difference between the chamber pressure and the magmastatic pressure, which can be obtained by integrating the conduit density over its length and multiplying by the acceleration due to gravity. From the inversion, the chamber overpressure ranged from 6 to 23 MPa with a mean of 16 MPa and the MAP model yielding 19 MPa. In contrast, most models in Anderson and Segall (2013) predict overpressures below 10 MPa. This difference arises from the large increase in viscosity as the magma crystallizes (Figure 12g), the effect of which was previously not accounted for.

Second, the coefficient of friction along the conduit margins tends to be lower than experimental estimates. These models correlate with small conduit radii and low chamber pressures in order to fit the observed extrusion flux. Notably, the MAP model has a coefficient of friction that agrees with experiments and a moderate chamber pressure—its large radius compensates for those effects to control volume flux. Moderately low coefficients of friction might result from the presence of unconsolidated fault gouge (Lavallée et al., 2014) and even frictional melting (Kendrick et al., 2012). It should be noted that momentum balance only resolves shear strength on the conduit walls τ_R, given by $\tau_R = f(\sigma - p_{hyd})$, where f is the coefficient of friction, σ is the normal stress acting on the conduit walls, and p_{hyd} is pore pressure, assumed to be hydrostatic. We also assumed lithostatic normal stress on the conduit walls, but topographic and tectonic stresses may decrease the normal stress below this value. In addition, the assumption of hydrostatic pore pressure is likely to be an underestimate. If gas is lost from the conduit to a reservoir at hydrostatic pore pressure, the resulting pore pressure acting on the conduit margin must necessarily be above hydrostatic. A substantial decrease in the effective normal stress would allow a higher coefficient of friction to maintain the same wall shear stress.

Results from both the sensitivity analyses and the Bayesian inversion also show that different combinations of model parameters can produce essentially the same predicted data. For example, models with higher chamber pressure may be indistinguishable from those with higher volatile content, because both produce similar observables. It may prove difficult to untangle contributions of individual parameters in an inversion. Solving the problem with a stochastic approach explores the range of possible models by allowing different parameter combinations. We can generally predict trade-offs between parameter combinations from the monotonic trends examined in the sensitivity analysis (Appendix B) and have developed better understanding of the implications of nonmonotonic behavior in the predicted data from varying k_c.

6.2. Evaluating Model Assumptions

In formulating the forward model, we made assumptions relating to constitutive laws, boundary conditions, and other model characteristics. These assumptions will undoubtedly influence response of the model to certain parameters; thus, it is meaningful to discuss their effects and relevance. Anderson and Segall (2013) already addressed issues relating to basic conduit geometry and model setup, noting that while the 1-D cylindrical conduit model is simplified, the approximation should provide first-order understanding of conduit processes. In reality, conduits may contain irregularities which can affect magma ascent behavior. In places where the conduit is narrowed, magma velocity must increase to preserve mass flux. This velocity increase requires the magnitudes of shear stress and pressure gradient to increase (equations (1) and (2)) and may alter the depth of plug formation due to the nonlinear dependence on strain rate, viscosity, and frictional sliding on the shear stress.

This study removes some assumptions made in Anderson and Segall (2013), although in doing so, we had to make additional approximations. To model crystallization, we approximate the system assuming isothermal equilibrium crystallization based on MELTS (Ghiorso & Sack, 1995; Schneider et al., 2012). This approach ignores crystallization kinetics. If crystallization kinetics lag behind the decompression timescale, we would not expect solids to be in equilibrium with the melt. Kozono and Koyaguchi (2012) estimate a crystal growth timescale of 10^4–10^5 s from experiments in Couch et al. (2003) on samples from Soufriere Hills Volcano. In our

model, decompression times are of the order of 10^8 s, considerably longer than this crystal growth timescale, suggesting that the assumption of equilibrium crystallization is valid for the 2004–2008 eruption of Mount St. Helens.

We quantify the strain rate dependence of the effect of solids on magma viscosity (Costa, 2005) using empirical equations from Caricchi et al. (2007). We estimate the strain rate assuming Newtonian flow, which may be inconsistent with the resulting nonlinear bulk rheology. We anticipate that the average strain rates ($\sim 10^{-5}$ s^{-1}) are good to an order of magnitude and do not expect large departures of viscosity from the Newtonian model as long as strain rates remain below the shear thinning limit of the magma, $\dot{\epsilon}_{st} \sim 10^{-3} G/\max(\eta_m) \approx 10^{-3} \cdot 10^{10}/10^8 = 10^{-1}$ s^{-1} (Gonnermann & Manga, 2007), where G is the magma shear modulus and is on the order of 10 GPa (Dingwell & Webb, 1989). This assumption fails as the flow becomes more plug like and strain becomes concentrated along the plug margins. We model this shear localization as a switch from Newtonian flow to rate-dependent frictional sliding, beyond which magma viscosity no longer plays a role in momentum balance. This model for shear localization is clearly an enormous simplification of the actual process and warrants additional study.

On a broader level, this model has made simplifications to study conduit flow on a 1-D macroscopic scale. We do not explicitly address effects of crystal and bubble dynamics on magma motion, although some have suggested that these microscopic interactions may exert strong controls on eruption style (e.g., Suckale et al., 2011). Additionally, advances in computing power have made 2-D or 3-D simulations of conduit flow possible. These studies have provided insight into lateral variations of magma properties and processes occurring close to the conduit wall such as cooling, and they also permit the study of noncylindrical conduits (e.g., Collier & Neuberg, 2006; Collombet, 2009). These models are relatively computationally intensive and may be unsuitable for the large number of iterations required by the MCMC inversion. However, they can be used to test assumptions made in this study.

7. Conclusions

We have applied a physics-based conduit model to the quasi steady state phase of the Mount St. Helens 2004–2008 eruption. By analyzing observations from the eruption in the context of a physics-based model, we obtain useful constraints on mechanical and chemical properties of the magmatic system.

1. The predicted mass flux shows a strong dependence on the efficiency of gas escape, due to effect of gas loss on porosity and bulk density. In some low-permeability cases, slight increases in pressure lead to a dramatic increase in mass flux when limited gas escape feeds back to decrease bulk density, further increasing ascent velocity.
2. The forward model exhibits nonunique behavior at low chamber pressure and low magma permeability, due to the same feedback between ascent rate, gas escape, and density.
3. Different gas escape regimes occur depending on the relative importance of lateral and vertical gas flow. Magma porosity can either increase or decrease in the upper conduit when vertical gas flow dominates, while lateral gas flow always decreases porosity. Competition between these two processes causes the nonmonotonic trend in exit velocity as magma permeability increases. For the wall rock permeability model of Manning and Ingebritsen (1999), the gas escape regime changes from dominantly lateral gas escape to vertical gas escape at $k_{mag}/k_{wall} \simeq 10^4$.
4. The forward model predicts diverse geophysical, petrologic, and geologic data, including dome rock porosity, exit velocity, and flux, as well as plug and solidus depth, all of which can be compared to observations at erupting volcanoes.
5. Results from the Bayesian inversion indicate that magma from the 2004–2008 eruption of Mount St. Helens had low (<5 wt %) volatile contents and that magma permeability is constrained to scale as $10^{-11.4}$ m^2 given the wall rock permeability model used here.
6. Chamber overpressures tend to be higher compared to previous studies to compensate for higher magma viscous resistance, and low wall friction coefficients also moderate the effect of viscous resistance to ensure that magma extrusion is maintained at the observed rate.

With results from the steady state system, we have developed a better understanding of interactions among conduit processes. Future work will implement the time-dependent model to explain transient observations throughout the eruption. Time-dependent effects include the unsteady term in the continuity equations (equations (3)–(5)), as well as time-varying boundary conditions at the conduit base. Future work will use GPS

and extrusion flux data to constrain model parameters to understand how subsurface magmatic processes influence the evolution of effusive eruptions.

Appendix A: Numerical Algorithm for Forward Model

The forward model consists of momentum balance (1) and three continuity equations (3)–(5). We write the continuity equations as

$$\frac{\mathrm{d}f(z, y)}{\mathrm{d}z} = g(z, y), \tag{A1}$$

where $\mathrm{d}f(z, y)/\mathrm{d}z$ describes the mass flux of constituents in terms of the fields $y(z) = [p, v, \phi_g, m_h]$, and $g(z, y)$ are source terms. The governing equations can be solved through various means, of which we choose the shooting method which can accommodate any loss of smoothness in the solution due to, for example, the percolation threshold. First, we apply the chain rule on (A1) to obtain implicit ordinary differential equations (ODEs),

$$\frac{\partial f(z, y)}{\partial y}\frac{\mathrm{d}y}{\mathrm{d}z} + \frac{\partial f(z, y)}{\partial z} - g(z, y) = 0. \tag{A2}$$

Experiments have shown that solving the momentum balance equation (1) at each ODE solver stage is faster and more robust than letting the implicit ODE method solve it. Solving the momentum balance first using a root-finding algorithm gives an estimate of the pressure gradient, denoted $\mathrm{d}p^*/\mathrm{d}z$. Combining

$$\frac{\mathrm{d}p}{\mathrm{d}z} - \frac{\mathrm{d}p^*}{\mathrm{d}z} = 0, \tag{A3}$$

with the continuity equation (A2) yields an implicit ODE system of the form

$$F\left(y, \frac{\mathrm{d}y}{\mathrm{d}z}, z\right) = 0. \tag{A4}$$

Initial conditions are given by the boundary conditions at the conduit base $y_{ch} = [p_{ch}, v_{ch}, \phi_g^{ch}, m_h^{ch}]$, and then y is integrated to the surface. As described in section 2.3, additional constraints are employed to relate ϕ_g^{ch} and m_h^{ch} to the total water and carbon dioxide contents at the conduit base. The shooting method solves equation (A4) for different v_{ch} and outputs a scalar quantity that measures the difference between the calculated surface pressure and atmospheric pressure,

$$\mathcal{F}_s(v_{ch}) = p(z = 0) - p_{atm}. \tag{A5}$$

A solution is obtained when $\mathcal{F}_s(v_{ch}) = 0$.

We use MATLAB's `ode15i` to solve (A4) and `fzero` to solve (A5). The function `ode15i` may be called multiple times in one computation of the solution due to the presence of discontinuities as discussed in section 2.4. Segments are computed using event functions called by `ode15i` that identify the percolation threshold and plug depths.

Appendix B: Sensitivity Tests of Model Parameters

We perform sensitivity tests exploring model parameter values posited by data from the Mount St. Helens eruption (Figure B1). In some cases, exit velocity and porosity are inconsistent with effusive eruptive behavior and therefore represent nonphysical solutions, but these cases still provide insight into the forward model. Correlations exist among the predicted data. Higher exit porosity corresponds to higher exit flux and exit velocity, but trends for plug depth and solidus depth are more complicated. With the exception of k_c, changes in other model parameters lead to essentially monotonic changes in predicted data.

Changes in the observables due to variations in conduit base pressure p_{ch}, nominal friction coefficient f_0, and conduit radius R can be interpreted directly from the momentum balance equation (1). Increasing the chamber pressure raises the overall pressure gradient. Reducing f_0, which translates directly into a drop in the
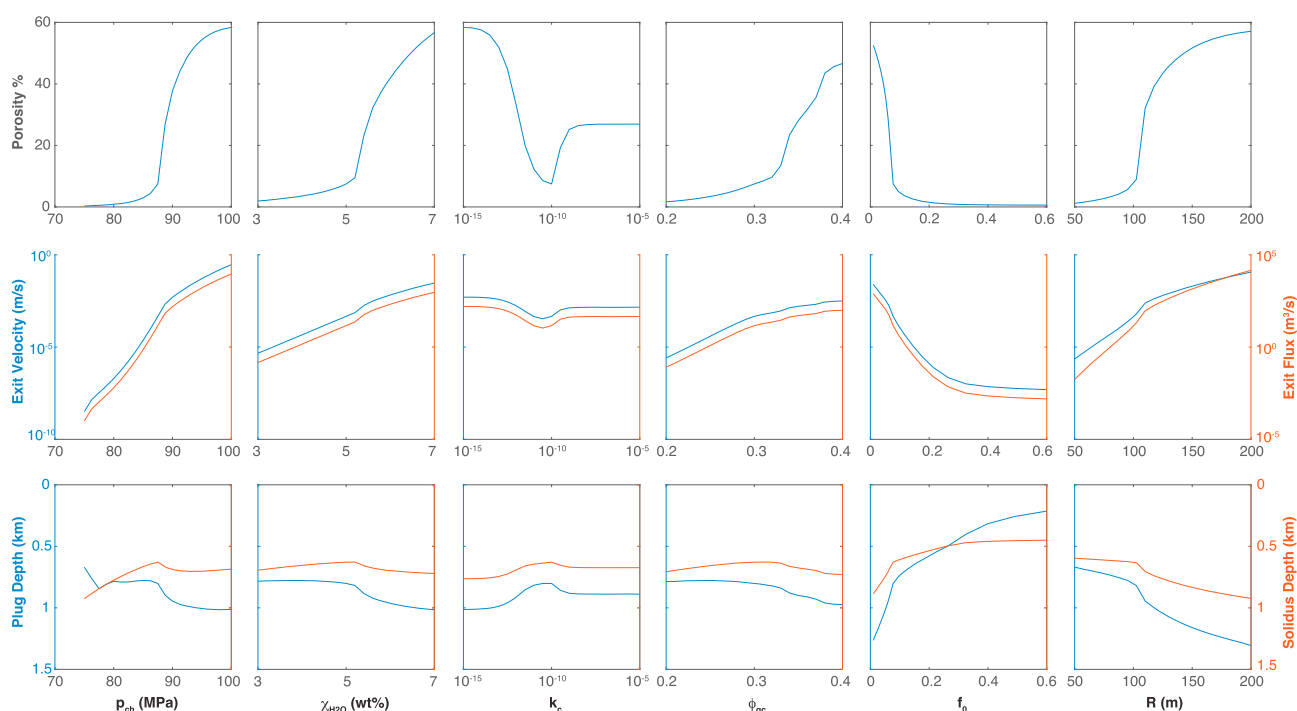
Figure B1. Sensitivity analysis for model parameters, showing predicted data obtained by varying one parameter at a time over the a priori range while holding all others at the value in Figure 4. Each column shows the range in each model parameter, while each row corresponds to predicted data. (top row) Dome rock porosity. (second row) Left (blue) axis shows exit velocity, while right (red) axis shows exit flux. (bottom row) Left (blue) axis shows plug depth, while the right (red) axis shows solidus depth.

friction coefficient, decreases shear resistance to flow along the conduit walls. A larger conduit radius reduces drag per unit volume of flow. All three effects increase magma velocity, which in turn increases the strain rate, limits viscosity increase due to solids at high solid fraction (Figure 2b), and also restricts degassing.

Total water content χ_h and magma permeability constants k_c, ϕ_{gc} directly affect the amount of exsolved volatiles within the conduit. At a chamber pressure of 87.5 MPa and total CO_2 content of 2,000 ppm, only 3.5 wt % water can be dissolved at the conduit base (Liu et al., 2005). Naturally, higher total water content increases the exsolved water content (porosity), decreases the density, and thus increases exit velocity and flux. Higher percolation threshold causes more exsolved volatiles to be retained in the conduit, again increasing exit velocity, flux, and porosity. The scaling constant for magma permeability k_c exhibits nonmonotonic trends in predicted data, which was discussed in section 3.3.

Plug depth and solidus depth show more complicated behavior; however, in general, both tend to be deeper at high porosity, exit velocity, and flux. The plug depth marks the transition from viscous flow to plug flow where wall shear stress reaches its peak (Figure 4b). At higher flow velocity (e.g., due to higher chamber pressure), the wall shear stress in the viscous flow regime is correspondingly larger (equation (1)) and increases dramatically at greater depth. The friction coefficient also increases due to the direct velocity-strengthening effect. The combined effect of these two changes causes the peak in shear stress to occur at greater depth in the conduit. The solidus depth is defined as the maximum z for which $\phi_l(z) = 0$. This depth should be shallower than the plug transition depth because the plug can effectively slide as a single mass while still containing some liquid melt. Given an isothermal conduit at 850°C, the solidus pressure is fixed at 24.6 MPa (Figure 2). The depth corresponding to this pressure depends on the density profile and viscous pressure losses. When porosity is higher, magma density decreases, so the solidus pressure of 24.6 MPa tends to occur at greater depth.

Appendix C: Constraints on Model Parameters and Data in Bayesian Inversion

For the inversion, we prescribe a priori constraints on the model parameters and errors in the data. These are discussed in detail below and are also summarized in Table 2.

C1. Constraints on the Prior

Boundary conditions at the conduit base are pressure and total water content. Total CO_2 content is fixed in this work. For calculations here we assume a conduit length of 3.5 km, close to the best fit model found by Anderson and Segall (2013). Changing the conduit length requires only a scaling of the pressure. Pressure at the conduit base is constrained at the lower bound by magmastatic pressure and on the upper bound by strength of the wall rock. For reference, an average dacite density of 2,400 kg/m^3 gives magmastatic pressure at the conduit base of 82.4 MPa (Whittington et al., 2009). Since we do not know the magma density a priori as it depends on porosity, we apply a conservative lower bound of 75 MPa. Since evidence suggests that magma did not fracture the surrounding rock, we assume that pressure there cannot greatly exceed lithostatic (92.7 MPa), as in Anderson and Segall (2013), giving an upper bound of 100 MPa.

Estimates from gas emissions during the eruption and petrologic analysis of amphiboles in the erupted dacite indicate that the magma reservoir contained $\sim$ 4 wt % dissolved water (Gerlach et al., 2008; Rutherford & Devine, 2008). Lower water content found in matrix glass and melt inclusions suggests that these inclusions were not well sealed (Blundy et al., 2008; Pallister et al., 2008). Because these data only constrain the dissolved water content as opposed to the total water content, we take the a priori total water content at the conduit base to range from 3 to 7 wt %.

We also estimate conduit radius in the inversion, assuming a constant cross section with depth. Observations of dome growth in Vallance et al. (2008) and Schilling et al. (2008) suggest a radius of $\sim$ 100 m. We consider a generous range to be 50 to 200 m.

Gas loss from the conduit requires estimation of two parameters: the scaling constant for magma permeability k_c and the percolation threshold ϕ_{gc}. The scaling constant is not well-constrained a priori, so we adopt a logarithmic scaling and use a range of 10^{-15}–10^{-5} m^2 (Kozono & Koyaguchi, 2012). Most experiments suggest that the percolation threshold for spherical bubbles is $\sim$30% (Blower, 2001; Klug & Cashman, 1996; Saar & Manga, 1999), however, the bubble size distribution may modify this value. For example, in polydisperse bubble size distributions, percolation threshold can be reduced to 27% (Blower, 2001). To be conservative, we take the range of ϕ_{gc} to be from 0.2 to 0.4.

Finally, we estimate the frictional properties of the conduit walls. Since extrusion velocity is assumed at steady state, the model is insensitive to the rate dependence of friction a, so we fix it to a typical value of 0.01 (Rice et al., 2001). We maintain the rate-dependent formulation so that we may later apply it to the time-dependent system, where the plug velocity changes with time. Given a, bounds on f_0 effectively fix bounds on f. Moore et al. (2008) conducted laboratory experiments to estimate frictional properties of the fault gouge on the margin of the Mount St. Helens plug. Under confining stresses of 96–195 kPa, they estimate a friction coefficient of 0.42–0.47. Note that these confining pressures are much lower than pressures expected in the conduit above the solidus depth (11–25 MPa). Since f_0 is a positive quantity, we set its prior in logarithmic space, from 10^{-2} to 0.6, in part based on preliminary runs.

C2. Data From the Eruption

The forward model and data likelihood in Bayes' theorem allow us to incorporate diverse data types naturally. In the steady state system, we use data from (1) porosity of extruded lava, (2) spine exit velocity, (3) spine exit volume flux, (4) plug depth, and (5) solidus depth.

Dense dacite samples, likely from the dome interior, have a porosity less than 10%, while vesicular dacite samples from dome margins have a porosity in the range 25–40% (Cashman et al., 2008; Kendrick et al., 2012; Smith et al., 2011; Thornber et al., 2008). Since our model is radially averaged and the high porosity samples are localized at the conduit margin, we judge a reasonable range of plug porosity to be from 5% to 10%.

From aerial and terrestrial photogrammetry, linear extrusion rate during the quasi-steady extrusion phase in March to December 2005 was 3–7×10^{-5} m/s (Major et al., 2008; Vallance et al., 2008). During the same period, the eruption flux was obtained independently by differencing sequential digital elevation models and found to be 1–2 m^3/s (Schilling et al., 2008). Assuming that conduit radius does not change substantially, these two observations are consistent with a radius of 75–150 m.

Plug depth represents the transition from a dominantly viscous flow regime to a frictional sliding regime. The best constraint on plug depth comes from the maximum depth of "drumbeat earthquakes," periodic earthquakes occurring beneath the dome during the eruption (Iverson et al., 2006). One interpretation for

these earthquakes, which we subscribe to, is that they are produced by stick-slip motion on the plug margins. While there are considerable uncertainties in depth, all drumbeat earthquakes appeared to originate from less than 1 km depth (Iverson et al., 2006; Moore et al., 2008; Thelen et al., 2008). Generous bounds on the depth of plug formation are from 1.5 to 0.5 km.

Petrologic studies constrain the pressure of the solidus, since much of the crystallization is the result of decompression rather than cooling (Cashman et al., 2008). The presence of tridymite in water-saturated, anorthite-free melts restricts pressure for matrix crystallization to 11–25 MPa (Cashman et al., 2008; Pallister et al., 2008). Coprecipitation of quartz and feldspar requires low pressures, around 5–10 MPa, corresponding to approximately 400–500 m depth (Cashman et al., 2008). These data confine the depth of crystallization to 0.5–1 km (Pallister et al., 2008). In the forward model, we define and solve for the solidus depth, above which no more melt exists ($\phi_l(z) = 0$). The solidus depth depends on the pressure gradient in the conduit but should be slightly shallower than plug depth, as the plug may form with some liquid melt present, and thus we estimate the same bounds of 1.5–0.5 km.

References

Anderson, K. R., & Poland, M. P. (2016). Bayesian estimation of magma supply, storage, and eruption rates using a multiphysical volcano model: Kilauea Volcano, 2000–2012. *Earth and Planetary Science Letters*, *447*, 161–171. https://doi.org/10.1016/j.epsl.2016.04.029

Anderson, K., & Segall, P. (2011). Physics-based models of ground deformation and extrusion rate at effusively erupting volcanoes. *Journal of Geophysical Research*, *116*, 1–20. https://doi.org/10.1029/2010JB007939

Anderson, K., & Segall, P. (2013). Bayesian inversion of data from effusive volcanic eruptions using physics-based models: Application to Mount St. Helens 2004–2008. *Journal of Geophysical Research: Solid Earth*, *118*, 2017–2037. https://doi.org/10.1002/jgrb.50169

Behrens, H., Zhang, Y., & Xu, Z. (2004). H_2O diffusion in dacitic and andesitic melts. *Geochimica et Cosmochimica Acta*, *68*(24), 5139–5150. https://doi.org/10.1016/j.gca.2004.07.008

Blower, J. (2001). Factors controlling permeability-porosity relationships in magma. *Bulletin of Volcanology*, *63*, 497–504. https://doi.org/10.1007/s004450100172

Blundy, J., Cashman, K. V., & Berlo, K. (2008). Evolving magma storage conditions beneath Mount St. Helens inferred from chemical variations in melt inclusions from the 1980–1986 and current (2004–2006) eruptions, *A volcano rekindled: The renewed eruption of Mount St. Helens, 2004–2006* (pp. 755–790). Reston, VA: U.S. Geological Survey Professional Paper 1750, U.S. Department of the Interior.

Byerlee, J. (1978). Friction of rocks. *Pure and Applied Geophysics PAGEOPH*, *116*, 615–626. https://doi.org/10.1007/BF00876528

Caricchi, L., Burlini, L., Ulmer, P., Gerya, T., Vassalli, M., & Papale, P. (2007). Non-Newtonian rheology of crystal-bearing magmas and implications for magma ascent dynamics. *Earth and Planetary Science Letters*, *264*(3–4), 402–419. https://doi.org/10.1016/j.epsl.2007.09.032

Cashman, K. V., Thornber, C., & Pallister, J. S. (2008). From dome to dust: Shallow crystallization and fragmentation of conduit magma during the 2004–2006 dome extrusion of Mount St. Helens, Washington, *A volcano rekindled: The renewed eruption of Mount St. Helens, 2004–2006* (pp. 387–413). U.S. Geological Survey Professional Paper 1750, U.S. Department of the Interior.

Collier, L., & Neuberg, J. (2006). Incorporating seismic observations into 2D conduit flow modeling. *Journal of Volcanology and Geothermal Research*, *152*(3–4), 331–346. https://doi.org/10.1016/j.jvolgeores.2005.11.009

Collombet, M. (2009). Two-dimensional gas loss for silicic magma flows: Toward more realistic numerical models. *Geophysical Journal International*, *177*(1), 309–318. https://doi.org/10.1111/j.1365-246X.2008.04086.x

Costa, A. (2005). Viscosity of high crystal content melts: Dependence on solid fraction. *Geophysical Research Letters*, *32*, 1–5. https://doi.org/10.1029/2005GL024303

Costa, A., Melnik, O., & Sparks, R. S. J. (2007). Controls of conduit geometry and wallrock elasticity on lava dome eruptions. *Earth and Planetary Science Letters*, *260*(1–2), 137–151. https://doi.org/10.1016/j.epsl.2007.05.024

Couch, S., Sparks, R. S. J., & Carroll, M. R. (2003). The kinetics of degassing-induced crystallization at Soufriere Hills volcano, Montserrat. *Journal of Petrology*, *44*(8), 1477–1502. https://doi.org/10.1093/petrology/44.8.1477

Dingwell, D. B., & Webb, S. L. (1989). Structural relaxation in silicate melts and non-Newtonian melt rheology in geologic processes. *Physics and Chemistry of Minerals*, *16*(5), 508–516. https://doi.org/10.1007/BF00197020

Gerlach, B. T. M., Mcgee, K. A., & Doukas, M. P. (2008). Emission rates of CO_2, SO_2, and H_2S, scrubbing, and preeruption excess volatiles at Mount St. Helens, 2004–2005. In *A Volcano Rekindled: The Renewed Eruption of Mount St. Helens, 2004–2006* (pp. 543–571). U.S. Geological Survey Professional Paper 1750, U.S. Department of the Interior.

Ghiorso, M. S., & Sack, R. O. (1995). Chemical mass transfer in magmatic processes IV. A revised and internally consistent thermodynamic model for the interpolation and extrapolation of liquid-solid equilibria in magmatic systems at elevated temperatures and pressures. *Contributions to Mineralogy and Petrology*, *119*(2–3), 197–212. https://doi.org/10.1007/BF00307281

Gonnermann, H. M., & Manga, M. (2007). The fluid mechanics inside a volcano. *Annual Review of Fluid Mechanics*, *39*, 321–356. https://doi.org/10.1146/annurev.fluid.39.050905.110207

Gonnermann, H. M., & Manga, M. (2013). Dynamics of magma ascent in the volcanic conduit. In *Modelling volcanic processes: The physics and mathematics of volcanism* (pp. 55–84).

Hastings, W. K. (1970). Monte Carlo sampling methods using Markov chains and their applications. *Biometrika*, *57*(1), 97–109.

Hess, K. U., & Dingwell, D. B. (1996). Viscosities of hydrous leucogranitic melts: A non-Arrhenian model. *American Mineralogist*, *81*, 1297–1300.

Iverson, R. M., Dzurisin, D., Gardner, C. A., Gerlach, T. M., Lahusen, R. G., Lisowski, M., … Vallance, J. W. (2006). Dynamics of seismogenic volcanic extrusion at Mount St Helens in 2004–05. *Nature*, *444*(1), 439–443. https://doi.org/10.1038/nature05322

Jaupart, C., & Allègre, C. J. (1991). Gas content, eruption rate and instabilities of eruption regime in silicic volcanoes. *Earth and Planetary Science Letters*, *102*(3–4), 413–429. https://doi.org/10.1016/0012-821X(91)90032-D

Kendrick, J. E., Lavallèe, Y., Ferk, A., Perugini, D., Leonhardt, R., & Dingwell, D. B. (2012). Extreme frictional processes in the volcanic conduit of Mount St. Helens (USA) during the 2004–2008 eruption. *Journal of Structural Geology*, *38*, 61–76. https://doi.org/10.1016/j.jsg.2011.10.003

Klug, C., & Cashman, K. V. (1996). Permeability development in vesiculating magmas: Implications for fragmentation. *Bulletin of Volcanology*, *58*, 87–100. https://doi.org/10.1007/s004450050128

Kozono, T., & Koyaguchi, T. (2010). A simple formula for calculating porosity of magma in volcanic conduits during dome-forming eruptions. *Earth, Planets and Space*, *62*(5), 483–488. https://doi.org/10.5047/eps.2010.02.005

Kozono, T., & Koyaguchi, T. (2012). Effects of gas escape and crystallization on the complexity of conduit flow dynamics during lava dome eruptions. *Journal of Geophysical Research*, *117*, 1–18. https://doi.org/10.1029/2012JB009343

Lavallée, Y., Hirose, T., Kendrick, J. E., De Angelis, S., Petrakova, L., Hornby, A. J., & Dingwell, D. B. (2014). A frictional law for volcanic ash gouge. *Earth and Planetary Science Letters*, *400*, 177–183. https://doi.org/10.1016/j.epsl.2014.05.023

Lejeune, A.-M., & Richet, P. (1995). Rheology of crystal-bearing silicate melts: An experimental study at high viscosities. *Journal of Geophysical Research*, *100*(B3), 4215–4229. https://doi.org/10.1029/94JB02985

Liu, Y., Zhang, Y., & Behrens, H. (2005). Solubility of H_2O in rhyolitic melts at low pressures and a new empirical model for mixed H_2O-CO_2 solubility in rhyolitic melts. *Journal of Volcanology and Geothermal Research*, *143*(1–3), 219–235. https://doi.org/10.1016/j.jvolgeores.2004.09.019

Llewellin, E. W., & Manga, M. (2005). Bubble suspension rheology and implications for conduit flow. *Journal of Volcanology and Geothermal Research*, *143*(1–3), 205–217. https://doi.org/10.1016/j.jvolgeores.2004.09.018

Mader, H. M., Llewellin, E. W., & Mueller, S. P. (2013). The rheology of two-phase magmas: A review and analysis. *Journal of Volcanology and Geothermal Research*, *257*, 135–158. https://doi.org/10.1016/j.jvolgeores.2013.02.014

Major, J. J., Kingsbury, C. G., Poland, M. P., & Lahusen, R. G. (2008). Extrusion rate of the Mount St. Helens lava dome estimated from terrestrial imagery, November 2004–December 2005. In *A Volcano Rekindled: The Renewed Eruption of Mount St. Helens, 2004–2006* (pp. 237–255). U.S. Geological Survey Professional Paper 1750, U.S. Department of the Interior.

Manning, C. E., & Ingebritsen, S. E. (1999). Permeability of the continental crust: Implications of geothermal data and metamorphic systems. *Reviews of Geophysics*, *37*(1), 127–150.

Mastin, L. G. (2002). Insights into volcanic conduit flow from an open-source numerical model. *Geochemistry, Geophysics, Geosystems*, *3*(7), 1–18.

Melnik, O., & Sparks, R. S. J. (1999). Nonlinear dynamics of lava dome extrusion. *Nature*, *402*(6757), 37–41. https://doi.org/10.1038/46950

Melnik, O., & Sparks, R. S. J. (2002). Dynamics of magma ascent and lava extrusion at Soufriere Hills Volcano, Montserrat. *Geological Society, London, Memoirs*, *21*(1), 153–171. https://doi.org/10.1144/GSL.MEM.2002.021.01.07

Melnik, O., & Sparks, R. S. J. (2005). Controls on conduit magma flow dynamics during lava dome building eruptions. *Journal of Geophysical Research*, *110*(2), 1–21. https://doi.org/10.1029/2004JB003183

Metropolis, N., Rosenbluth, A. W., Rosenbluth, M. N., Teller, A. H., & Teller, E. (1953). Equation of state calculations by fast computing machines. *The Journal of Chemical Physics*, *21*(6), 1087–1092. https://doi.org/doi:10.1063/1.1699114

Michaut, C., Bercovici, D., & Sparks, R. S. J. (2009). Ascent and compaction of gas rich magma and the effects of hysteretic permeability. *Earth and Planetary Science Letters*, *282*(1–4), 258–267. https://doi.org/10.1016/j.epsl.2009.03.026

Moore, P. L., Iverson, N. R., & Iverson, R. M. (2008). Frictional properties of the Mount St. Helens gouge. In *A Volcano Rekindled: The Renewed Eruption of Mount St. Helens, 2004–2006* (pp. 415–424). Vancouver, WA: U.S. Geological Survey Professional Paper 1750.

Mosegaard, K., & Tarantola, A. (1995). Monte Carlo sampling of solutions to inverse problems. *Journal of Geophysical Research*, *100*(B7), 12,431–12,447. https://doi.org/10.1029/94JB03097

Pallister, B. J. S., Thornber, C. R., Cashman, K. V., Clynne, M. A., Lowers, H. A., Mandeville, C. W., Brownfield, I. K., & Meeker, G. P. (2008). Petrology of the 2004–2006 Mount St. Helens lava dome—Implications for magmatic plumbing and eruption triggering. In *A Volcano Rekindled: The Renewed Eruption of Mount St. Helens, 2004–2006* (pp. 647–702). U.S. Geological Survey Professional Paper 1750, U.S. Department of the Interior.

Rice, J. R., Lapusta, N., & Ranjith, K. (2001). Rate and state dependent friction and the stability of sliding between elastically deformable solids. *Journal of the Mechanics and Physics of Solids*, *49*(9), 1865–1898. https://doi.org/10.1016/S0022-5096(01)00042-4

Rust, A. C., & Cashman, K. V. (2004). Permeability of vesicular silicic magma: Inertial and hysteresis effects. *Earth and Planetary Science Letters*, *228*(1–2), 93–107. https://doi.org/10.1016/j.epsl.2004.09.025

Rutherford, M. J., & Devine, J. D. (2008). Magmatic conditions and processes in the storage zone of the 2004–2006 Mount St. Helens dacite, *A Volcano Rekindled: The Renewed Eruption of Mount St. Helens, 2004–2006* (pp. 703–725). U.S. Geological Survey Professional Paper 1750, U.S. Department of the Interior.

Saar, M. O., & Manga, M. (1999). Permeability-porosity relationship in vesicular basalts. *Geophysical Research Letters*, *26*(1), 111–114. https://doi.org/10.1029/1998GL900256

Schilling, S. P., Thompson, R., Messerich, J., & Iwatsubo, E. Y. (2008). Use of digital aerophotogrammetry to determine rates of lava dome growth, Mount St. Helens, Washington, 2004–2005. In *A Volcano Rekindled: The Renewed Eruption of Mount St. Helens, 2004–2006* (pp. 145–167). U.S. Geological Survey Professional Paper 1750, U.S. Department of the Interior.

Schneider, A., Rempel, A. W., & Cashman, K. V. (2012). Conduit degassing and thermal controls on eruption styles at Mount St. Helens. *Earth and Planetary Science Letters*, *357–358*, 347–354. https://doi.org/10.1016/j.epsl.2012.09.045

Smith, R., Sammonds, P. R., Tuffen, H., & Meredith, P. G. (2011). Evolution of the mechanics of the 2004–2008 Mt. St. Helens lava dome with time and temperature. *Earth and Planetary Science Letters*, *307*(1–2), 191–200. https://doi.org/10.1016/j.epsl.2011.04.044

Sparks, R. S. J. (2003). Forecasting volcanic eruptions. *Earth and Planetary Science Letters*, *210*, 1–15. https://doi.org/10.1016/S0012-821X(03)00124-9

Suckale, J., Hager, B. H., Elkins-Tanton, L. T., & Nave, J.-C. (2011). It takes three to tango: 2. Bubble dynamics in basaltic volcanoes and ramifications for modeling normal Strombolian activity. *Journal of Geophysical Research*, *116*, B06208. https://doi.org/10.1029/2011JB008351

Thelen, W. A., Crosson, R. S., & Creager, K. C. (2008). Absolute and relative location of earthquakes at Mount St. Helens, Washington, using continuous data: Implications for magmatic processes. In *A Volcano Rekindled: The Renewed Eruption of Mount St. Helens, 2004–2006* (pp. 71–95). U.S. Geological Survey Professional Paper 1750, U.S. Department of the Interior.

Thornber, B. C. R., Pallister, J. S., Rowe, M. C., Mcconnell, S., Herriott, T. M., Eckberg, A., . . . Knaack, C. M. (2008). Catalog of Mount St. Helens 2004–2007 dome samples with major- and trace-element chemistry: U.S. Geological Survey open-file report 2008-1130 (Tech. Rep.). Vancouver, WA: U.S. Geological Survey.

Vallance, J., Schneider, D., & Schilling, S. (2008). Growth of the 2004–2006 lava-dome complex at Mount St. Helens, Washington. In *A volcano rekindled: The renewed eruption of Mount St. Helens, 2004–2006* (pp. 169–208). U.S. Geological Survey Professional Paper 1750, U.S. Department of the Interior.

Whittington, A. G., Hellwig, B. M., Behrens, H., Joachim, B., Stechern, A., & Vetere, F. (2009). The viscosity of hydrous dacitic liquids: Implications for the rheology of evolving silicic magmas. *Bulletin of Volcanology*, *71*(2), 185–199. https://doi.org/10.1007/s00445-008-0217-y